

Strain Estimator in Ultrasound Elastography Using Multiple Frames

by

A M K Muntasir Shamim

**MASTER OF SCIENCE
IN
ELECTRICAL AND ELECTRONIC ENGINEERING**



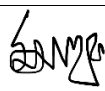

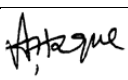


Department of Electrical and Electronic Engineering
Islamic University of Technology (IUT)
Board Bazar, Gazipur-1704, Bangladesh
July 2021

© 2021 A M K Muntasir Shamim
All Rights Reserved

CERTIFICATE OF APPROVAL

The thesis titled ‘Strain Estimator in Ultrasound Elastography Using Multiple Frames.’ submitted by **A M K Muntasir Shamim**, St. No. 181021008 of academic year 2018-19 has been found as satisfactory and accepted as partial fulfillment of the requirements for the Degree of MASTER OF SCIENCE IN ELECTRICAL AND ELECTRONIC ENGINEERING on **30 July 2021**.

1. 	Chairman
Prof. Dr. Md. Ruhul Amin (Supervisor) Professor and Head Department of Electrical and Electronic Engineering Islamic University of Technology (IUT), Gazipur.	
2. 	Member (Ex-officio)
Prof. Dr. Md. Ruhul Amin (Supervisor) Head Department of Electrical and Electronic Engineering Islamic University of Technology (IUT), Gazipur.	
3. 	Member
Prof. Dr. Md. Ashraful Hoque Professor and Dean Faculty of Engineering Department of Electrical and Electronic Engineering Islamic University of Technology (IUT), Gazipur.	
4. 	Member
Prof. Dr. Mohammad Rakibul Islam Professor Department of Electrical and Electronic Engineering Islamic University of Technology (IUT), Gazipur.	
5. 	Member (External)
Prof. Dr. Md. Aynal Haque Professor Department of Electrical and Electronic Engineering Bangladesh University of Engineering and Technology (BUET) Dhaka	

Declaration of Candidate

It is hereby declared that this thesis report or any part of it has not been submitted elsewhere for the award of any Degree or Diploma and it has not been copied from other person's work.



A M K Muntasir Shamim
Student No.:181021008
Academic Year: 2018-19
Date: July 28, 2021

Dedicated
to
my late mother
who is always in spirit with me.

Table of Contents

CERTIFICATE OF APPROVAL	ii
Declaration of Candidate.....	iii
Table of Contents	v
List of Figures	viii
List of Tables.....	x
List of Abbreviations.....	xi
Acknowledgment	xii
Abstract	xiii
1 INTRODUCTION	1
1.1 Ultrasound Imaging.....	1
1.2 Elastography	2
1.3 Literature Review	4
1.4 The motivation of the Thesis.....	5
1.5 The objective of the Thesis	6
1.6 The Organization of the Thesis	6
2 STATE OF THE ART STRAIN ESTIMATION TECHNIQUES	8
2.1 Gradient-Based Cross-Correlation Techniques For Strain Estimation	8
2.2 Short-Term Correlation-Based Strain Estimation Techniques.....	9
2.3 Two-Dimensional Strain Estimation Techniques.....	10
2.4 Adaptive Stretching Based Strain Estimation Techniques.....	11
2.5 Spectral Based Strain Estimation Techniques.....	11
2.6 Zero-Phase Detection of Complex Cross-Correlation Function-Based Strain Estimation Techniques	12
2.7 Sub-Sampled Displacement Tracking Based Strain Estimation Techniques.....	13
2.8 Cost-Function Minimization Schemes-Based Strain Estimation Techniques.....	13
2.9 Direct Strain Estimation Techniques:.....	14
2.10 Multi-Level Block Matching Algorithm-Based Strain Estimation Techniques:..	15
2.11 Optical Flow-Based Strain Estimation Techniques.....	17
2.12 Strain Estimation Techniques Using Multiple Frames.....	18
3 PROPOSED TECHNIQUES	20
3.1 Frame selection.....	20
3.2 Conversion of RF to B-mode or envelope mode.....	22
3.3 Optical Flow-based Multi-Frame Strain Estimator	22
3.3.1 Stage 1: Motion estimation between Frame 1 and Frame 2.....	23

Step 1: Motion Estimation Between Frame F1 And F2 Through Block Matching	23
Step 2: Displacement Error Correction and Strain Estimation from Displacements	25
Step 3: Registering Strain to Pre-Compression Frame Size	26
Step 4: Unwarping Frame 2	29
Step 5: Optical Flow Between Unwarped Frame 2 And Frame 1:	31
Horn-Shunck Optical Flow:	32
Step 6: Strain Estimation from Optical Flow Estimates:	34
Step 7: Stage 1 Strain Estimation	34
3.3.2 Stage 2: Introducing the Third Frame in The Algorithm	36
Step 8: Choosing Frame 3 Slightly After Frame 2	36
Step 9: Warping Frame 2	36
Step 10: Finer Displacement Estimation Between Warped Frame 2 And Frame 3 Through Optical Flow	37
Step 11: Strain Estimation from Optical Flow Vectors	38
Step 12: Final Strain Estimation:	39
3.4 Multistage Optical Flow-Based Multi-Frame Strain Estimator	41
3.4.1 Multistage Motion Estimation	41
3.4.2 Multistage Strain Estimation and Registration	45
4 RESULTS	49
4.1 Finite Element Simulation:	49
4.1.1 Processing Parameters	50
4.1.2 Strain Images	51
4.1.3 Performance Indices	55
4.1.3.1 Signal to Noise Ratio	56
4.1.3.2 Contrast to Noise Ratio	57
4.1.4 Performance Analysis	61
4.2 Patient Data/In-vivo Data	62
4.2.1 Processing Parameters	62
4.2.2 Patient 1	64
4.2.3 Patient 2	65
4.2.4 Patient 3	66
4.2.5 Patient 4	67
4.2.6 Performance Analysis	68
5 DISCUSSION and CONCLUSION	69
5.1 Discussions	69
5.2 Conclusion	70
5.3 Future Perspectives	71

References 72

List of Figures

1.1 Application of stress in a phantom to depict varying tissue elasticity [24].	3
2.1 Echo time delay computation through the processing of pre and post compression signals. [30]	9
2.2 Two-step optical flow method for elastography.[15]	18
3.1 Selection of frames after compression.	21
3.2 Conversion of RF to B-mode Source. [49]	22
3.3 Motion estimation by block matching.	24
3.4 Size comparison in pixels.	25
3.5 Strain registration with iterative extrapolation.	27
3.6 Bicubic interpolation grid.	28
3.7 Unwarping frame 2	30
3.8 Optical flow between unwarped Frame 2 and Frame 1.	31
3.9 Strain estimation at stage 1.	35
3.10 Warping post-compression frame F2.	37
3.11 Finer displacement estimation between warped frame 2 and frame 3.	38
3.12 Final strain estimation of optical flow-based multi-frame (OFMF) strain estimator.	39
3.13 Flowchart of optical flow-based multi-frame (OFMF) strain estimator.	40
3.14 Scaling down processing parameters before repositioning.	43
3.15 Motion estimation after repositioning search window - x_1' and y_1' represent reference lateral and axial displacements from previous stage respectively; X_1 and Y_1 represent lateral and axial displacement to be estimated in current stage respectively.	43
3.16 Vector summation of the multistage displacements.	44
3.17 Flow of the multistage motion estimation.	45
3.18 Registration of multistage strain matrices to frame.	47
3.19 Flowchart of multi-stage optical flow-based multi-frame (MSOFMF) strain estimator.	48
4.1 Ideal elastogram from finite element simulation.	50
4.2 Maximum NCC maps at 3 rd stage and 4 th stage.	51
4.3 Strain Images of Optical flow-based Multi-Frame (OFMF) Strain Estimator at (a) 2% (b)4% (c) 8% (d) 12% (e) 16% applied strain.	52

4.4 Strain Images of Multistage Optical Flow based Multi Frame (MSOFMF) Strain Estimator at (a) 2% (b)4% (c) 8% (d) 12% (e) 16% applied strain.	54
4.5 Strain images comparison of various algorithms.	55
4.6 SNR comparison between various strain estimators.	56
4.7 CNR comparison of the top lesion.	57
4.8 CNR comparison of the centre inclusion.	58
4.9 CNR comparison of the bottom left inclusion.	59
4.10 CNR comparison of the bottom right inclusion.	60
4.11 Patient 1-(a). Log compressed B-mode image, Elastogram using - (b) MSOFMF (c) OFMF (d) 2D least squares method with uniform temporal stretching, (e) 1D least squares method with uniform temporal stretching (f) 1D spectral adaptive stretching strain estimators.	64
4.12 Patient 2-(a). Log compressed B-mode image, - (a). Log compressed B-mode image, Elastogram using - (b) MSOFMF (c) OFMF (d) 2D least squares method with uniform temporal stretching, (e) 1D least squares method with uniform temporal stretching (f) 1D spectral adaptive stretching strain estimators.	65
4.13 Patient 3-(a). Log compressed B-mode image, Elastogram using - (b) MSOFMF (c) OFMF (d) 2D least squares method with uniform temporal stretching, (e) 1D least squares method with uniform temporal stretching (f) 1D spectral adaptive stretching strain estimators.	66
4.14 Patient 4-(a). Log compressed B-mode image, Elastogram using - (b) MSOFMF (c) OFMF (d) 2D least squares method with uniform temporal stretching, (e) 1D least squares method with uniform temporal stretching (f) 1D spectral adaptive stretching strain estimators.	67
4.15 SNR comparison of patient data cases	68

List of Tables

4.1 Processing parameters for finite element simulation.	50
4.2 SNR comparison between various strain estimators.	56
4.3 CNR comparison of the top lesion.	57
4.4 CNR comparison of the centre inclusion.	58
4.5 CNR comparison of the bottom left inclusion.	59
4.6 CNR comparison of the bottom right inclusion.	60
4.7 Processing parameters at different stages of multistage motion estimation	62
4.8 SNR comparison of patient data cases.	68

List of Abbreviations

1D	One Dimensional
2D	Two Dimensional
AM	Analytic Minimization
AS	Adaptive Stretching
B-mode	Brightness mode
CNR	Contrast to Noise Ratio
CT	Computer Tomography
FEM	Finite Element Method
GPU	Graphical Processing Unit
MLBM	Multi-level block matching
MRI	Magnetic Resonance Imaging
MSOFMF	Multistage Optical Flow-based multi-Frame
OF	Optical Flow
OFMF	Optical Flow-based multi-Frame
PET	Positron Emission Tomography
RF	Radio Frequency
ROI	Region of Interest
SE	Strain Estimator
SNR	Signal to Noise Ratio
TDE	Time Delay Error

Acknowledgment

First and foremost, I would like to express my deepest gratitude to Allah (SWT) for providing me with the necessary ability and fortitude to carry out this research work.

Without the help and encouragement of several wonderful people, I would not have been able to finish this thesis. Hence, I would like to take this opportunity to show my appreciation to those who have assisted me in a myriad of ways.

I would like to express my sincerest gratitude to Dr. Md Ruhul Amin, my thesis advisor, for his steadfast support and guidance during this project. I could not have asked for a more supportive and considerate supervisor. He was always willing to sit and listen to my concerns, and he made me feel like my effort was worthwhile. The fact that he was ready to offer me so much of his time and expertise was a significant influence in completing this thesis. I also really appreciate him for allowing me to pursue research independently and widen my vision in medical imaging.

I would also like to thank Dr. Kaisar Alam for being a great mentor to me in ultrasound elastography and providing me access to the patient data sets.

I also would like to thank the examination committee members for allowing me to present this work. I am also grateful to all the faculty members of the electrical and electronic engineering department, Islamic University of Technology (IUT), for their support and inspiration during my course and thesis work

I want to convey my heartfelt thanks to my father, grandmother, and family for their unwavering moral support during this project. It would not have been feasible for me to go this far without their help and sacrifice.

And finally, the one person who has made this all possible has been my beloved late mother. Her memories and dreams are always with me as a constant source of support and encouragement. She made an untold number of sacrifices working as a selfless doctor and inspired me to work in the medical field to serve humanity better.

Abstract

Accuracy of the motion estimation, higher resolution, robustness to noise and decorrelation arising from out-of-plane motion, faster execution speeds, preciseness to be integrated into subsequent quantitative analysis algorithms are the desired outcomes of a well-established strain estimation algorithm suited for ultrasound elastography. Two strain estimation approaches based on multiple frames that integrate optical flow have been presented to address the primary limitations of existing methodologies. These two proposed techniques attempt to increase the accuracy of displacement estimates, increase spatial resolution over existing methods, and be immune to noise caused by signal decorrelation arising due to the rapid oscillation of RF data and error propagation. Both the techniques use the envelope form of RF data, i.e., B-mode data which is less impacted by signal decorrelation and produce axial frame-sized strain estimates. The proposed techniques were tested on finite element simulation data and in-vivo/patient data. Our techniques statistically outperformed other well-established strain estimators in terms of performance, i.e., SNR and CNR. Even at higher applied compressions like 8% and 16% our proposed methods are highly effective and usable where the other algorithms fail terribly. Spatial resolution was increased by a factor of ~30 than the other algorithms making elastograms similar in dimensions to the frame size.

Chapter 1

INTRODUCTION

Medical imaging is the harbinger to that future when diagnosing and treating patients without negative side effects is feasible. Medical imaging depicts what is going on inside the human body without the need for surgery or other invasive procedures. It can be employed for both diagnosis and remedial purposes. To date, various medical imaging modalities such as Computer Tomography (CT), Magnetic Resonance Imaging (MRI), Ultrasound, X-ray and others have been used in various medical anatomies to obtain qualitative and quantitative information that can be used for diagnostic purposes.

1.1 Ultrasound Imaging

Ultrasound imaging uses high-frequency sound waves to visualize the internal regions of the human body. A conducting gel is used to transfer high-frequency sound waves from an ultrasound probe to the body. The waves then bounce back when they strike the body's interior anatomical components, creating a real-time image. It is the most economical and widely available medical imaging modality. Ultrasound imaging captured in real time is able to show the movement of the interior organs of the human body as well as the flow of blood via the blood vessels. Ultrasound imaging, unlike X-ray or CT imaging, does not expose patients to ionizing radiation. This modality is now widely utilized in prenatal imaging, as well as cardiac imaging, breast cancer diagnosis, and the identification of benign and malignant tissues in the human body, owing to the low risks involved. One of the most researched aspects of Ultrasound Imaging is Ultrasound Elastography.

1.2 Elastography

Ultrasonographic elastography is a noninvasive method for determining the relative stiffness or displacement (strain) of tissue in response to applied force [1]. It deals with observing and processing the tissue response to infer the mechanical properties of the tissue and then displaying the results to the operator. Elastography delineates the elastic properties and stiffness of investigated tissue in an illustrative pictorial map [1].

Elastography is esteemed superiorly for its real-time processing, execution speed, portability, inexpensiveness, and ubiquitous accessibility. Being completely noninvasive, this imaging modality can acquire essential diagnostic information in contrast to a mere anatomical image.

The use of US elastography for tissue imaging was originally reported in 1987. Since its inception, elastography has been adopted for the initial medical prognosis of various disease conditions in many organs like breasts, liver, thyroids etc. In the last two decades, the use of real-time commercially available clinical ultrasound machines has spurred an outburst of research into potential oncologic and non-oncologic clinical applications of Ultrasound Elastography. The hypothesis that contributed to the emergence of elastography was that there is a substantial difference in soft tissue modulus between normal and diseased tissues. The underlying concept is inferring the presence or status of disease based on the investigated tissue stiffness. Predominantly the diseased organs are stiffer than healthy ones based on the pieces of evidence of scirrhous breast carcinomas, which are found to be extremely hard nodules[2], and liver tissues with cirrhosis that are stiffer than the regular counterpart [3].

In recent years, elastography-based strain imaging methods have garnered a lot of interest for their noninvasive evaluation of tissue mechanical characteristics that may be utilized to diagnose a variety of clinical diseases. Ultrasound-based techniques are particularly appealing because of their many intrinsic benefits, including broad availability and cheap cost. A variety of ultrasonic elastography techniques have been developed, each utilizing a distinct excitation mechanism. Shear wave imaging uses ultrasound-generated traveling shear wave stimuli, while strain imaging uses internal or external compression stimuli. While ultrasound elastography has provided positive findings for noninvasive assessment of liver fibrosis since its inception,

diagnostic methods in breast [4]–[19], thyroid [20], prostate [21], kidney[22], and lymph node imaging [23] are also well-established and improving.

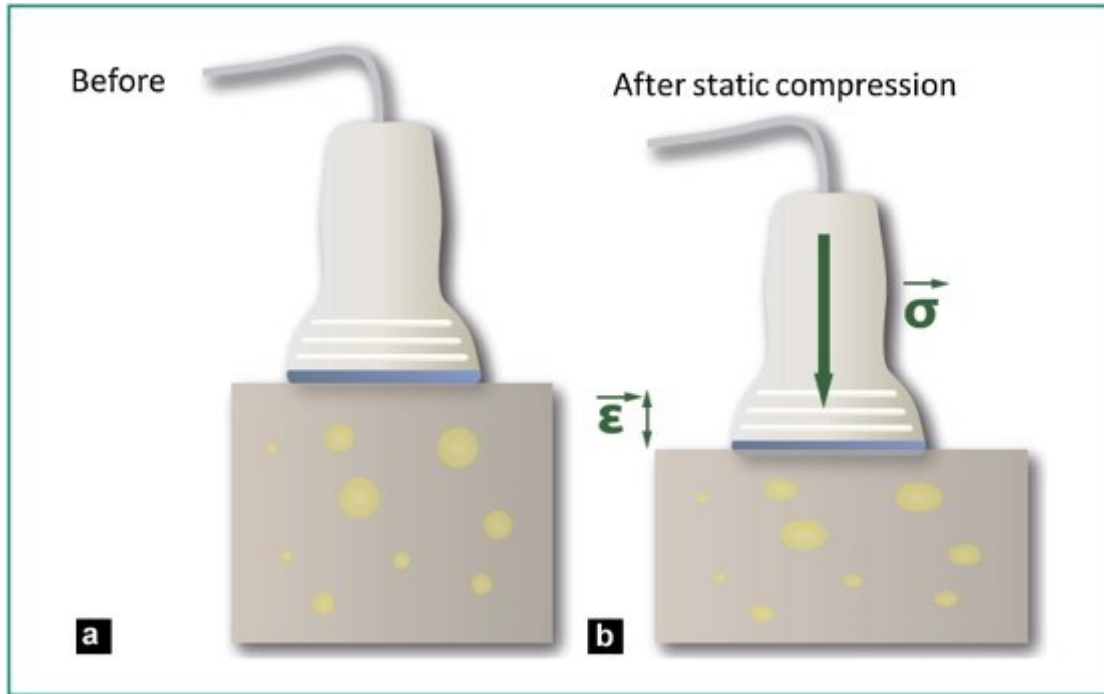


Fig. 1.1 Application of stress in a phantom to depict varying tissue elasticity [24].

Elastography has been analogized with the century-old manual palpation method [25]. But the manual palpation method is inhibited due to the dependence on the physicians' experience in explaining the intricate nature of the tissue and the inaccessibility to the deeper tissues in the body. Thus, quantifying these differences of stiffness and elastic modulus contrast between regular and pathological tissues in images of the tissue strain tensor or Young's modulus has been the impetus for developing this imaging approach.

Based on the type of force applied, the elastography can be classified broadly into two major groups, namely quasi-static elastography and dynamic elastography. Quasi-static elastography encompasses strain elastography techniques, and dynamic elastography consists of techniques like Acoustic Radiation Forced Impulse Imaging (ARFI), Transient elastography and, Shear Wave elastography. In this work, the topic for investigation is based on the quasi-static method.

The quasi-static method is the first strain elastography technique developed by the Ophir group at the beginning of 1990 [1]. Strain elastography reconstructs a 'Strain Map' by calculating the

deformations caused by applying static compression using an ultrasound probe by the operator. Since the beginning, the quasi-static method [18] has been employed to a wide variety of medical issues, from identifying and differentiating atherosclerotic plaques [27] to improving diagnosis of breast [4]–[19] and prostate cancer [28]–[30]. Motion is induced within the tissue using either an external or internal quasi-static mechanical source, and the resulting tissue deformation is measured using a suitable displacement estimator from the pre- and post-deformed radiofrequency (RF) echo frames; and finally, the induced tissue strains are computed using a finite-difference or least-squares strain estimator from the measured tissue deformations.

1.3 Literature Review

Various elastographic techniques have been employed from the inception of this ultrasound imaging modality to this date, and these techniques keep on evolving, aiming to overcome the issues faced by the previous methods. During the infancy of this modality, the strain was estimated from the gradient of the motion estimation of pre- and post-compression RF signals. The gradient-based methods [1], [5], [31] typically assume that the motion of the tissue due to the compression is only in the axial direction. These techniques suffer from lower resolution and are affected hugely by noise. Decorrelation is also a major challenge in ultrasound elastographic motion estimation which arises due to out-of-plane motion. Various techniques till today are affected by this decorrelation, and solutions like temporal stretching [32] and direct strain estimation [6]-[9] were proposed to improve the Signal to Noise ratio (SNR) of elastograms. These techniques involve finding a stretching factor based on the compression of the tissue.

Determining the amount of compression mathematically from free hand compression techniques is complicated and often not possible. In low compression cases stretching the post-compression signal leads to the accumulation of noise in stiff areas where the tissue displacement is small. Thus strain estimation techniques based on determining the stretch factors iteratively were introduced [33]-[34]. These are highly computationally expensive as it involves iteratively searching for the best stretch factor that produces the best strain elastograms. Owing to the varying stiffness of the examined tissue and the nature of data acquisition, lateral motion is also experienced by the tissue in addition to rotational, elevational,

axial motion due to free hand compression. Motion estimation techniques like [35]-[36] were developed to include the lateral motion in strain elastography to reduce motion propagation error and to correctly locate the displacements. For improving the precision of the displacement estimates subsample displacement layer is integrated with initial coarse displacements to achieve subsampled displacement accuracy in the order of micrometers [37]. The subsample estimation improves the accuracy of the motion estimation through reiteratively correlating pre and post deformation echo signals [4].

Increasing the spatial resolution of strain images is another challenge that has been extensively researched. Short-term correlation-based techniques [38] and multi-level approaches[39][40][41] has been employed in the quest for increased spatial resolution. Optical Flow-based methods [15] [42] have also been employed in strain elastography in conjunction with motion tracking by block matching to improve the accuracy of the motion estimation process using computationally expensive RF data.

Multiple-frames-based strain estimation techniques [11], [12] have also been utilized for combining several pictures in which two frames are examined at a time, and strains are computed sequentially to compound them. This lowers noise compared to the conventional two frame approach. These techniques are more computationally complex as RF data is used.

1.4 The motivation of the Thesis

Accuracy of the motion estimation, higher resolution, robustness to noise and decorrelation arising from out of plane motion, faster execution speeds, preciseness to be integrated into subsequent quantitative analysis algorithms are the desired outcomes of a well-established strain estimation algorithm suited for ultrasound elastography.

The motivation of the thesis was to improve our proposed techniques on the above-mentioned fronts. We aim to increase the performance metrics while implementing the algorithm in a less computationally expensive data form.

1.5 The objective of the Thesis

In this thesis work, first, the current techniques of ultrasound elastography and their limitations have been investigated. To overcome the main limitations of the current techniques, two strain estimation techniques based on multiple frames that incorporate optical flow have been proposed. These two proposed techniques aim to improve the accuracy of displacement estimates, improve the resolution from existing approaches and be immune to noises arising due to decorrelation and error propagation.

The objectives of our thesis can be outlined as follows:

1. Investigating the state of the art of strain estimation techniques and find out their contributions and limitations.
2. Increasing the SNR and CNR of strain images using multiple frames.
3. Increase the spatial resolution of the strain estimation through RF frame-sized strain estimation.
4. Improve the accuracy of motion estimation through optical flow based residual motion estimation of the displacement layer.
5. Reducing computational complexity of RF echo based elastographic techniques by using only B-mode/ envelope of pre- and post-compression echo signals.

1.6 The Organization of the Thesis

This thesis is organized according to the following:

Chapter 1 INTRODUCTION:

This chapter introduces strain elastography. A brief literature overview stating the current limitations is included. This is concluded by the objective of the thesis and thesis organization outlines.

Chapter 2 STATE OF THE ART STRAIN ESTIMATION TECHNIQUES:

Strain estimation techniques can be grouped under specific common working themes. In this chapter, the state-of-the-art strain estimation techniques are discussed elaborately, including their innovativeness and limitations.

Chapter 3 PROPOSED TECHNIQUES:

Two new strain estimation techniques using multiple frames based on the optical flow method are presented in this chapter. A summary of the working steps is illustrated with a flow chart at the end of each technique.

Chapter 4 RESULTS:

Strain images generated by the two proposed algorithms are depicted in this chapter. The strain images of other well-established algorithms are also presented for comparison. Later quantitative justification and comparison of these techniques are portrayed.

Chapter 5 DISCUSSION and CONCLUSION :

A summary of the thesis work is presented. Scopes for future approaches for progress are also discussed.

Chapter 2

STATE OF THE ART STRAIN ESTIMATION TECHNIQUES

Motion estimation is generally the most important step in quasi-static elastography. Various types of motion estimation strategies have been incorporated in quasi-static elastography from its inception. Generally, after motion tracking, strain estimation is performed. These techniques can be subdivided into some major categories, which are discussed below:

2.1 Gradient-Based Cross-Correlation Techniques For Strain Estimation

During the initial days, the strain profile in gradient-based method was generated along the transducer axis, which was then computed from the one-dimensional 1D cross-correlation analysis of pre and post-compression frame pair [1]. This method has been a steppingstone to modern-day ultrasound strain estimation techniques. This technique suffers from decorrelation and low resolution.

O'Donnell et al. demonstrated various ultrasound speckle tracking methods with the intent of permitting measurement of internal displacements through the cross-correlation-based method and strain maps over a wide-ranging tissue motion. Experiments using gelatin-based tissue-equivalent phantoms resulted in improved contrast resolution in strain elastograms. [13].

Ophir et al. showed that the finite difference computations of echo time-delay through the processing of pre- and post-compression echo signals can generate tissue strain elastograms [19].

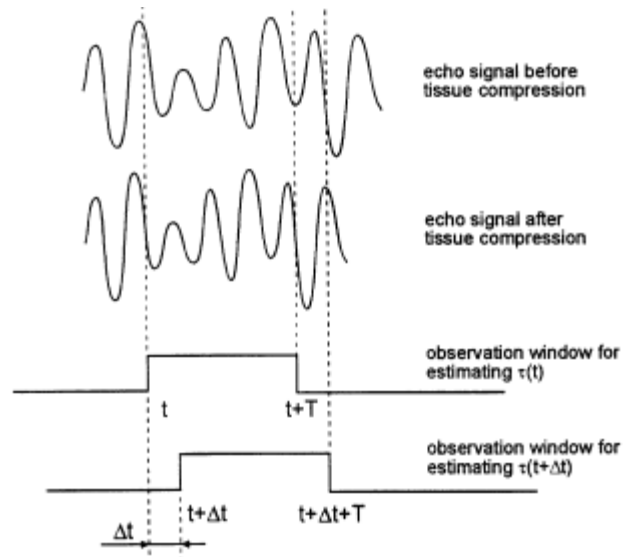


Fig. 2.1 Echo time delay computation through the processing of pre and post compression signals. [30]

Maximizing the low contrast detectability for soft biological tissues in elastography has been the goal of Bilgen et al. [5]. To achieve the goal, Bilgen et al. tweaked experimental settings and signal processing variables to obtain a sharp peak in the cross-correlation function, resulting in precise displacement estimations. They further claimed that stretching the post-compression echo can significantly increase the magnitude of the cross-correlation function, and preprocessing the compression echo signals can markedly reduce displacement errors [5].

Location of the peak of the cross-correlation function between gated pre-compression and post-compression signals form the time delay estimates. Good quality elastograms require accurate estimation of the time delays. Decorrelation of the echo signal arising due to tissue compression is the main source of time delay error (TDE). Kaisar et al. validates temporally stretching the post-compression echo signals before the TDE step(through 1D cross-correlation) reduce the decorrelation noise in elastograms [32].

2.2 Short-Term Correlation-Based Strain Estimation Techniques

In ultrasound imaging, the image resolution of elastograms is of paramount significance. However, the tradeoff that this imaging modality has to tolerate is of precision versus spatial resolution. Although a bigger correlation kernel reduces error variance, it also lowers the spatial

resolution. [38]. Strain decorrelation is another crucial cause of errors in displacements estimated by cross-correlation techniques. Thus, increasing spatial resolution without affecting the error variance and lowering the strain decorrelation errors has been a topic of research from earlier days.

In this aspect, Lubinski et al. introduced the concept of short term correlation where they demonstrated that reducing the correlation kernel can decrease the strain decorrelation error, and a higher SNR is attainable by filtration of the correlation functions before displacement estimation [38].

2.3 Two-Dimensional Strain Estimation Techniques

Brusseau et al. devised a 2-D locally regularized strain estimate technique that not only computes the ROI's 2-D translation motion but also takes axial size variation into account. [43] This technique identifies the unreliable displacement estimates as a function of the cross-correlation function and uses a regularization technique to correct them [43]. This method consists of initial motion computation of the change in the ROI position induced by the transducer and then ROI position refinement according to the initial motion computation. The axial scaling or stretching factor is estimated, and ROIs are scaled according to the sign of the scaling factor. Eventually, correction through regularization aids in axial strain computation. Finally, the combination of elastographic results culminates in a production of video frames depicting the tissue deformation induced by the stress.

The lateral and elevational components arising due to free hand compression are generally ignored, but they distort the axial strain estimate by generating decorrelation noise. Konofagou et al. propose a novel weighted interpolation technique acting across adjacent RF A-lines for high accuracy monitoring of the lateral motion [4]. These accurate lateral-displacement estimates allow for a fine correction for lateral decorrelation that taints axial motion estimates. The authors show the distribution of Poisson's ratios in the tissue by dividing the lateral elastogram by the axial elastogram.

2.4 Adaptive Stretching Based Strain Estimation Techniques

Adaptive stretching strain calculation methods [34] for ultrasound elasticity imaging aim to find out the stretch factors that maximize the correlation between the pre- and post-compressed RF signals by iteratively stretching the latter one. These then adopt the normal 1D cross-correlation method and gradient-based approach to generate the tissue strain image. This method produces elastograms with comparatively less noise than gradient-based approaches, but the imaging efficiency is low.

The window moving is added to simplify the calculations of the cross-correlation function, and an adaptive stretch factor method based on moving window for ultrasound elasticity imaging is proposed.[11]

Local tissue strain is calculated in ultrasound utilizing techniques like cross-correlation on local segments of RF data. [7]. Local data segments are chosen by multiplying RF data by a rectangle window in this procedure. Non-ideal spectral behavior is caused by such data truncation and this effect can be minimized by utilizing smooth windows. Rifat et al. found that smoothing windows improve the SNR and CNR of strain images [7].

2.5 Spectral Based Strain Estimation Techniques

Strain causes a time delay and time scaling in the received signal, similar to velocity. In elastography, time delay techniques are often employed to indirectly (through the displacement estimate) measure tissue strain caused by applied compression. According to Konofagou et al., the temporal scaling factor can be computed spectrally and used as a direct measure of strain[8]. The strain causes a Doppler-like frequency shift as well as a change in the bandwidth of the bandpass power spectrum of the echo signal. Two frequency shift strain estimators are discussed, which have been proven to be more robust but less accurate than time delay estimators in simulations and testing [8]. The spectral methods are less sensitive to phase decorrelation noise, which results in improved robustness.

Kaisar et al. presented a new spectral strain estimator that maximizes the correlation between the spectra of pre- and post-compression echo signals using iterative frequency-scaling of the

latter [44]; they also describe a variant of this method that is computationally more efficient but less accurate. In tests and 2-D finite-element simulations, the adaptive spectral strain estimator outperformed traditional estimators by combining the advantages of time- and frequency-domain techniques.

Cross-correlation methods are used in traditional spectrum elastographic techniques to measure strain. Despite promising outcomes, decorrelation effects restrict the precision of these techniques. Decorrelation effects become increasingly evident as tissue stresses increase because tissue compression in the time domain corresponds to upscaling in the frequency domain. They are a major concern in spectral cross-correlation elastography. A two-stage hybrid spectral elastographic method is presented by Hoyt et al. in one of his works [14]. The first stage is correcting for bandwidth widening (due to tissue compression) between pre- and post-compression power spectra pairs using an assumed spectral scaling factor (i.e., beginning strain estimate). Due to improper scaling factor selection in the first stage, the second phase uses spectral cross-correlation methods to compute any residual strain information. In simulation and testing, this novel hybrid spectral elastographic method was compared to both conventional spectral and adaptive temporal elastographic approaches. The hybrid spectral-based technique not only outperformed the conventional spectrum elastographic methodology, but it also outperformed the adaptive temporal-based elastographic approach.

2.6 Zero-Phase Detection of Complex Cross-Correlation Function-Based Strain Estimation Techniques

The key to measuring strain in ultrasonic elastography is the precise estimate of temporal displacements between two signals. A method [13] that calculates these displacements using phase differences of the associated base-band signals was previously presented. The computational efficiency of this method is a significant advantage over correlation approaches. An extension of the method is described by Pesavento et al. in [45] that iteratively takes into consideration the time shifts of the signals to address aliasing and accuracy issues in phase shift estimation. It was shown that the method is identical to searching for the correlation function's maximum. Furthermore, a robust logarithmic compression that simply compresses the signal's envelope was suggested as this compression introduces no systematic errors and lowers

decorrelation noise substantially. The resultant method is a computationally simple and quick replacement for traditional correlation algorithms, and strain image accuracy is enhanced.

Brusseau et al. devised an adaptive approach based on the estimate of strains as local scaling factors in order to expand the range of reliable strain measurements [46]. Because of its flexibility, this technique is well suited to calculating scaling factors for greater strains or a broad range of strain fluctuations. In the rest and stressed state echo signals, segments belonging to the same region of the tissue are adaptively chosen. Local scaling factors are then calculated by repeatedly changing their values until the phase of the complex cross-correlation function reaches zero.

2.7 Sub-Sampled Displacement Tracking Based Strain Estimation Techniques

A speckle tracking method that performs both axial and lateral motion estimates at the same time to increase the accuracy of displacement estimation was proposed [37]. Specifically, this method finds an iso-contour in the region of the highest correlation between two blocks of pre- and post-compression ultrasonic radiofrequency echo data using conventional ultrasound echo data. Locating the center of the correlation function's iso-contour is claimed to be equivalent to the undetermined (sub-sample) motion estimate.

2.8 Cost-Function Minimization Schemes-Based Strain Estimation Techniques

Rivaz et al. present a 2D strain imaging method based on dynamic programming to minimize a cost function [47]. The cost function considers echo amplitude similarity and displacement continuity. The inclusion of smoothness within the cost function reduces decorrelation noise because tissue deformations are smooth. As a result, the proposed method produces high-quality free-hand palpation elastography strain images with up to 10% compression demonstrating that

it is more resistant to signal decorrelation (caused by scatterer motion in high axial compression and nonaxial probe motions) than standard correlation techniques.

However, elastograms using this method show some stress concentration around the lesion which is not visible in the corresponding cross-correlation images. This might be an artifact, or high stresses are generated only around the lesion due to the nonlinear mechanical characteristics of the phantom.

Two real-time elastography methods based on analytic minimization (AM) of regularized cost functions are described.[48] The first technique (1D AM) generates axial strain and an integer lateral displacement, while the second method (2D AM) generates both axial and lateral stresses. Both AM techniques are resistant to minor decorrelations present across the elastogram since the cost functions include similarity of radiofrequency (RF) data intensity and displacement continuity. To make the approaches resistant to large local decorrelations, Rivaz et al. use techniques from robust statistics and include Kalman filtering, which is used to calculate the strain estimates from the motion field produced by AM techniques.[48]

2.9 Direct Strain Estimation Techniques

For high-quality average strain imaging, Arafat et al. developed gradient-based and direct strain estimating methods that incorporate cost function maximization [6]. Stiffness usually is a continuous function. Since stiffness is considered to be a continuous function, the stiffness of proximal tissues is almost identical to the stiffness of the tissue that corresponds to a particular data window. A cost function is generated using exponentially weighted nearby pre- and post-compression RF echo normalized cross-correlation peaks in the lateral (for displacement estimation) or axial and lateral (for direct strain measurement) directions. The average displacement/strain is obtained from the associated maximum cost function, ensuring a controlled continuity in displacement/strain. The tissue is displaced laterally as a consequence of axial stress. Therefore, Poisson's ratio was integrated to pick a suitable 1-D post-compression echo segment. Gradient-based strain computation considers two stretching factors at the same time, allowing for accurate imaging of lesions.

A phase-based direct average strain estimate technique is proposed by Sharmin et al. [17]. Direct axial strain is estimated by integrating the phase of the zero-lag cross-correlation

function between the segmented pre-deformation and stretched post-deformation echo signals. Unlike traditional phase-based strain estimators, which calculate strain from the displacement field, strain in this work is estimated in a single step utilizing the secant method and the direct phase-strain connection. As an alternative to utilizing the interrogative window's instantaneous phase to ensure strain continuity, an average phase model is designed using the phases of adjacent windows, assuming that the strain is basically identical in close vicinity to the interrogative window. This technique takes the impact of lateral shift into consideration but does not require a previous approximation of the applied strain.

Kamrul et al. describe a technique that takes use of the fact that the post-compression rf echo signal is a time-scaled and shifted copy of the pre-compression rf echo signal, like previous time/frequency domain methods. Unlike conventional techniques, this methodology computes the mean strain without explicitly utilizing any post-filter and/or prior local displacement/strain computations [9]. In the short-time Fourier transform domain, it is accomplished using a nearest-neighbor weighted least-squares-based Fourier spectrum equalization technique. Since the local tissue strain is expected to maintain continuity with its neighbors, the mean strain at the interrogative window can be calculated directly from the common stretching factor that aims to minimize a cost function deduced from the exponentially skewed pre- and post-compression RF echo signal in both the longitudinal and transverse directions.

2.10 Multi-Level Block Matching Algorithm-Based Strain Estimation Techniques:

Unlike single-level block matching, multi-level algorithms utilize a variable-size matching block and search window. Large block size is first employed to give a coarse-resolution approximation of the entire motion field. Each successive level utilizes a smaller block size and search window than the previous levels to improve spatial resolution without losing noise immunity. The multi-level approach is comparable to hierarchical systems employed in block matching algorithms for video coding [49]. These approaches vary in how they utilize various subsampling methods and cost function minimization.

In one approach, Fai Yeung et al. demonstrated multi-level block matching utilizing SSD as a cost function in continuous tissues [41]. The multi-level block matching (MLBM) method uses

varying matching-block and search-window sizes in a coarse-to-fine scheme, maintaining motion field information while keeping the relative immunity to noise associated with large matching blocks.

The ability of the 2D multi-level cross-correlation technique to calculate local displacement fields and stresses in discontinuous media is demonstrated by Varghese et al. [39]. Using a multi-level pyramid method, coarse displacement estimates are first produced using sub-sampled B-mode data. On the lowest level of the pyramid holding the RF echo signal data, the coarse displacement estimations are then used to guide the high-resolution estimation. This technique combines the benefits of B-mode envelope tracking's resilience with the accuracy of RF motion tracking to produce high-resolution displacement and strain estimations. The method can track discontinuous displacement fields thanks to the processing scheme presented in this article, which uses coarse displacement estimates utilizing B-mode data and a multi-level approach. As a result, the assumption of a continuous displacement field is not necessary in the multi-level technique, unlike previous strain estimation methods.

In this approach, the coarse displacement estimates are generated using a pyramidal processing method beginning with down-sampled B-mode pre- and post-compression picture pairings, where the cross-correlation cutoff is 0.3 in the first level resulting in poor guidance displacement estimates for subsequent levels. Although the method is reported to be quicker in terms of computing, the qualitative characteristics of elastograms in the following levels for breast lesion investigations suffer as a result. Errors in displacement estimations propagate in the early stages if they are large enough that the specified search areas do not include actual displacements. When tissue is squeezed, significant and irregular local deformation may occur owing to image collection constraints, resulting in local decorrelation and the buildup of spurious peaks in the calculation.

Meshram et al. implemented an accelerated GPU-based multi-level approach that is used for lagrangian carotid strain imaging based on Bayesian regularization [40]. In that technique, first, a cumulative displacement vector map is created using the predicted inter-frame displacements. Second, before estimating the appropriate cumulative strain tensors, accumulated displacement vectors are collected. The local strain tensors are then calculated using the gradient of the displacement vectors. This technique is based on the initial multi-level technique [39]. The addition of Bayesian regularization to correct the motion field is highly computationally

expensive, and thus the implementation of this algorithm using GPU was a notable work to speed up the process.

2.11 Optical Flow-Based Strain Estimation Techniques

A two-step Optical Flow method has been proposed by Xiaochang et al. to improve the performance of conventional optical flow method-based strain estimation [15]. The conventional OF technique is used in the first phase to calculate the displacements and stresses between the pre- and post-deformed RF signals. In the second step, the estimated axial stresses and axial shear strains are utilized to warp the pre-compression RF signals. The displacements and stresses between the warped pre-deformed RF signals and the post-deformed RF signals are then estimated using the OF method. The axial strains acquired in both stages are combined to produce the final axial strains. Xiaochang et al. incorporate local warping to improve the coherence between the pre- and post-deformed signals. This local warping technique is analogous to the aligning and stretching methods used in correlation-based elastography [5][32]. Xiaochang et al. suggest that by decreasing both bias and standard deviation, the warping method enhances the precision and accuracy of strain estimation.

The Optical flow algorithm [50] considers the intensity of the material point of the tissue in a complete RF sequence is always invariant. This assumption can be called intensity invariant constraint in terms of computer vision. The presence of speckle noises and tissue deformations, on the other hand, typically interferes negatively with the intensity restrictions, resulting in poor motion estimation results.

The two-step optical flow method incorporates both axial and shear strain parts to locally warp RF data. Although this technique is good for phantom simulations, these don't work well in patient data cases as there are a lot of intensity variations in the RF data, which consequently makes the local warping inconsistent.

The two-step optical flow method for elastography is illustrated in Fig. 2.2

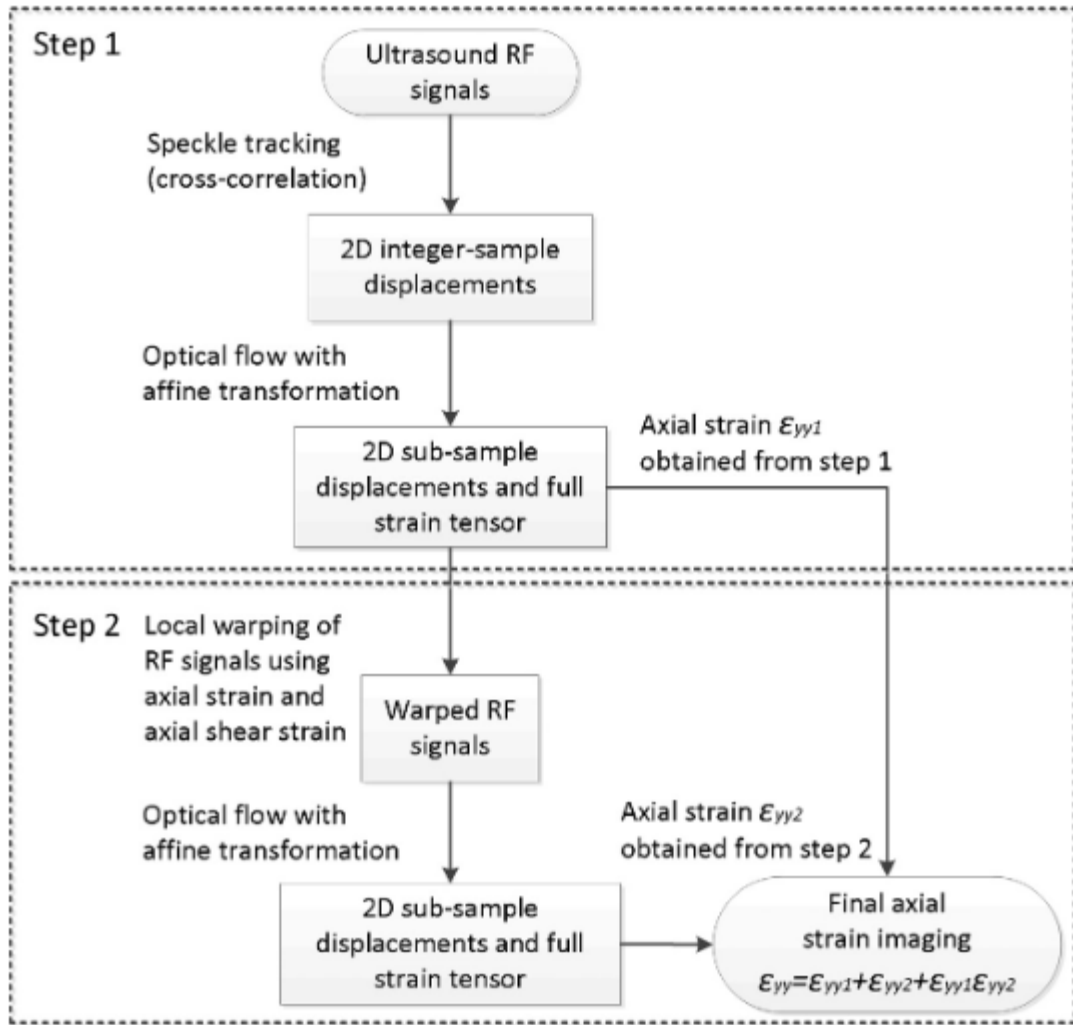


Fig. 2.2 Two-step optical flow method for elastography.[15]

2.12 Strain Estimation Techniques Using Multiple Frames

In order to compute a displacement field from three pictures, Rivaz et al. use material mechanics to establish limits on changes in the displacement field over time [12]. These restrictions are then utilized to create a regularized cost function that considers the amplitude similarity of three ultrasonic pictures and the continuity of displacement. In an expectation-maximization paradigm, the cost function is maximized and to reduce the impact of outliers, iteratively reweighted least squares is employed.

Rivaz et al. also describe an alternate method for combining several pictures in which two frames are examined at a time and strains are computed sequentially to compound them. This technique is shown to lower noise and removes ambiguity in displacement estimation when compared to utilizing two pictures or collecting strains.

Chapter 3

PROPOSED TECHNIQUES

In this work, to overcome the limitations of the current methods, two strain estimation techniques based on multiple frames have been proposed. The first method, titled “Optical flow-based multi-frame strain estimator”, is the skeleton of our idea. The second method, titled “Multistage optical flow-based multi-frame strain estimator”, is an improvement of the first method. In this chapter, we discuss the techniques behind these two algorithms.

3.1 Frame selection

The first step to generate elastograms is the selection of multiple good RF echo frames from the ultrasound RF sequence. Because most pairings of RF frames either do not show adequate deformation for obtaining relevant strain pictures or are significantly impacted by decorrelation, choosing suitable frames for the strain estimation process is critical. In this thesis work, three frames are selected based on their quality of producing good quality strain elastograms. Earlier experiences and prior data of choosing good frames were used for validating the algorithm on patient data cases.

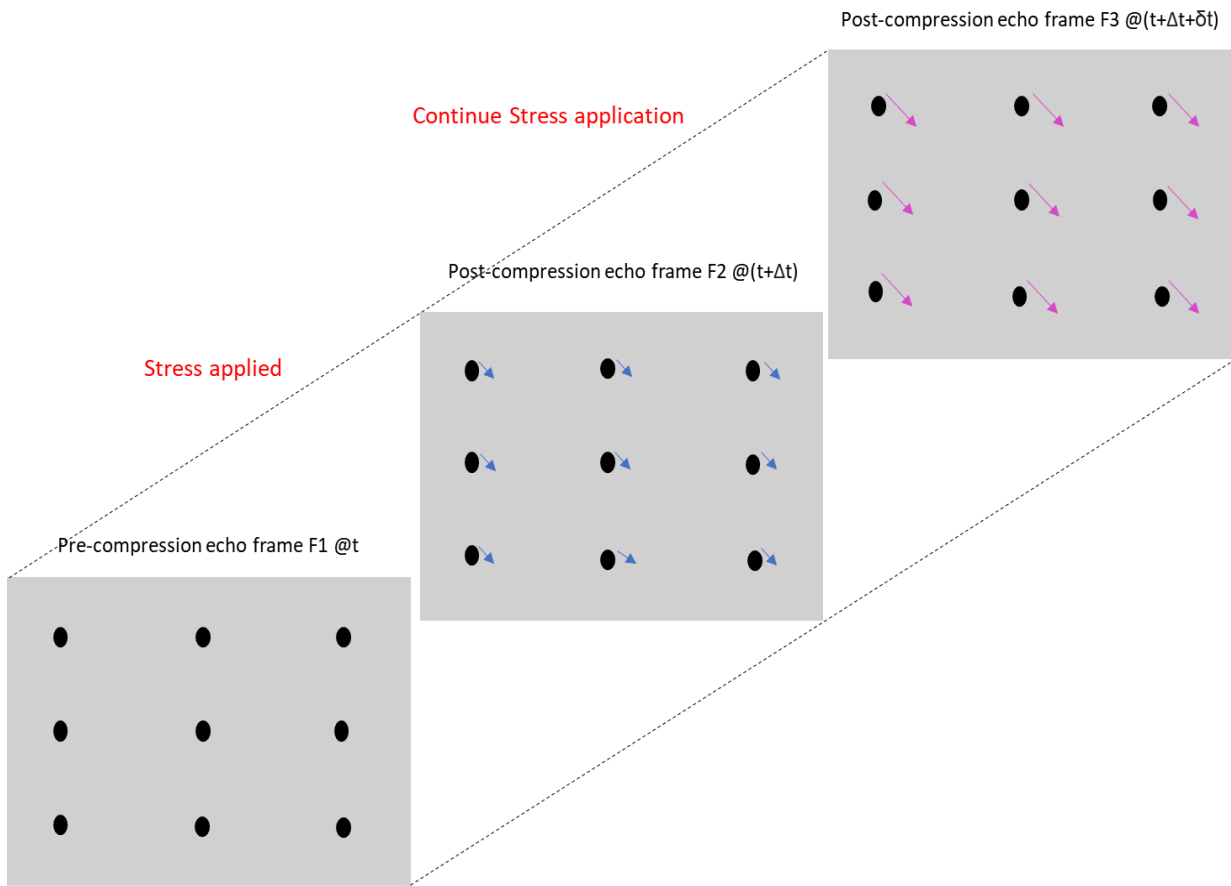


Fig. 3.1 Selection of frames after compression.

Fig. 3.1 demonstrates the timing of the selected frames. Pre compression echo frame F1 was chosen at time t before the application of stress. In quasi-static elastography, for the acquisition of post-compression data, stress is generally applied by the clinician perpendicular to the investigated tissue. After a certain interval Δt , post-compression echo frame F2 at a time $(t + \Delta t)$ is selected with prior knowledge. Under the application of the stress another post-compression frame, F3 is then selected after a smaller time interval of δt . Most of the deformation generally occurs before time $(t + \Delta t)$ i.e., at the onset of selecting F2 as the clinician stops implying more force at a certain stage. Thus, the deformation between F2 and F3 is less compared to that between F1 and F2. This nature of data acquisition has been exploited later in the algorithm.

3.2 Conversion of RF to B-mode or envelope mode

This step involves transforming the RF data form of the pre- and post-compression echo signal to the envelope or B-mode data using the Hilbert Transform, a known technique in asynchronous detectors that does not require center frequency. The B-mode image contains only the amplitude information along the axial direction when compared to the RF data and needs far less computational power to process. After the mapping of intensity and post-

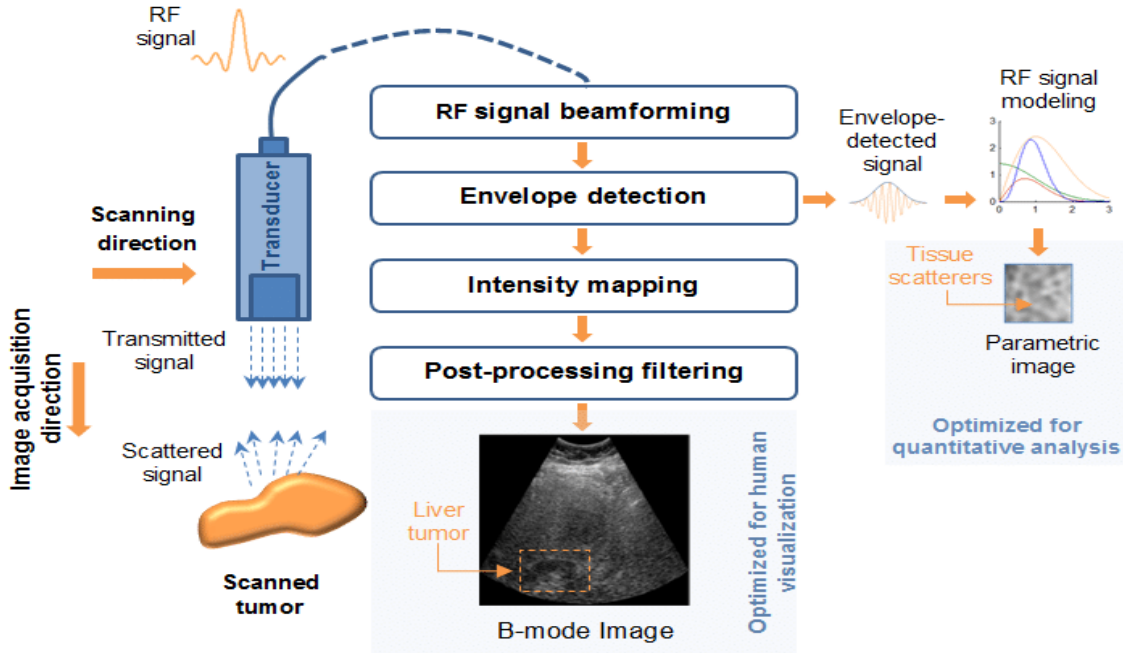


Fig. 3.2 Conversion of RF to B-mode Source. [49]

processing filtering, these frames become usable. Therefore, the algorithm is computationally optimized to work only with envelope form.

3.3 Optical Flow-based Multi-Frame Strain Estimator

The algorithm of this multi-frame strain estimator can be divided into two stages. The steps of each stage are first outlined here.

Stage 1

1. Motion estimation between Frame 1 and Frame 2 to find out displacements.
2. Displacement error correction and strain estimation from displacements
3. Registering strain to pre-compression frame size.
4. Unwarping frame 2 using displacements from step 1.

5. Finding optical flow vectors between unwarped frame 2 and frame 1.
6. Strain estimation from optical flow vectors.
7. Adding step 3 and 5 to finalize stage1 strain estimation.

Stage 2:

8. Choosing frame 3 slightly after frame 2.
9. Warping frame 2 to reconstruct a frame like frame 3 i.e., obtain warped frame 2.
10. Finer displacement estimation between warped Frame 2 by and Frame 3 through optical flow.
11. Strain estimation from optical flow vectors of step 10.
12. Generation of final strain image by adding step 7 and step 11.

The process in each step is described in detailed next.

3.3.1 Stage 1: Motion estimation between Frame 1 and Frame 2

Step 1: Motion Estimation Between Frame F1 And F2 Through Block Matching

Motion estimation due to the tissue deformation through block matching requires matching a kernel (matching 2D block) with a bigger 2D block called the search window to optimize the cost function. Generally SAD, SSD require cost factor minimization, but we chose 2D normalized cross-correlation to maximize the cost function.

Mathematically the 2D Normalized cross correlation function can be represented by equation 3.1

$$NCC(i, j) = \frac{\sum_{x=1}^M \sum_{y=1}^N [f(x, y) - \bar{f}][t(x + i, y + j) - \bar{t}]}{\sqrt{\sum_{x=1}^M \sum_{y=1}^N [f(x, y) - \bar{f}]^2 * \sum_{x=1}^M \sum_{y=1}^N [t(x + i, y + j) - \bar{t}]^2}} \quad 3.1$$

where f and t represent the pre- and post-compression data frames. i and j denote relative shifts between the f and t data frames, M and N are the block sizes in axial and lateral directions, where \bar{f} and \bar{t} denote the mean values of the intensities of the blocks f and used in the calculation.

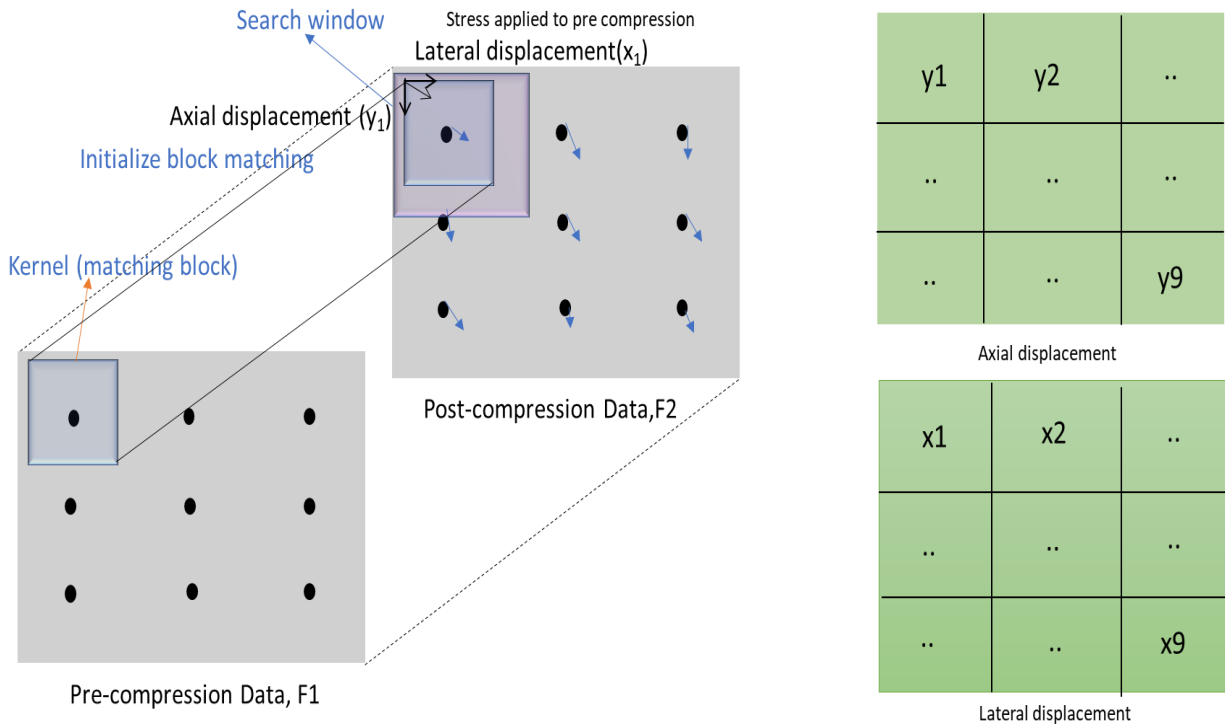


Fig. 3.3 Motion estimation by block matching.

Prior knowledge and empirical data were used for the choosing sizes of the processing parameters, i.e., axial, lateral sizes of kernels and search window and shifts. Sizes of kernel and search-window were carefully selected to maximize the cross-correlation function and thus have less impact on signal decorrelation. The corresponding displacement to this maximum similarity gives the crude peak displacements. Thus, sliding the kernels and search windows at a certain degree of overlap with pre-defined axial and lateral shifts, the initial displacement matrices are obtained. These matrices account for both the axial and lateral displacements of the initial stage obtained from the B-mode of the pre-compression echo F1 and post-compression F2 echo signal.

An approximate size comparison between the displacements and frame size for one of the cases of patient data can be shown according to Fig. 3.4.

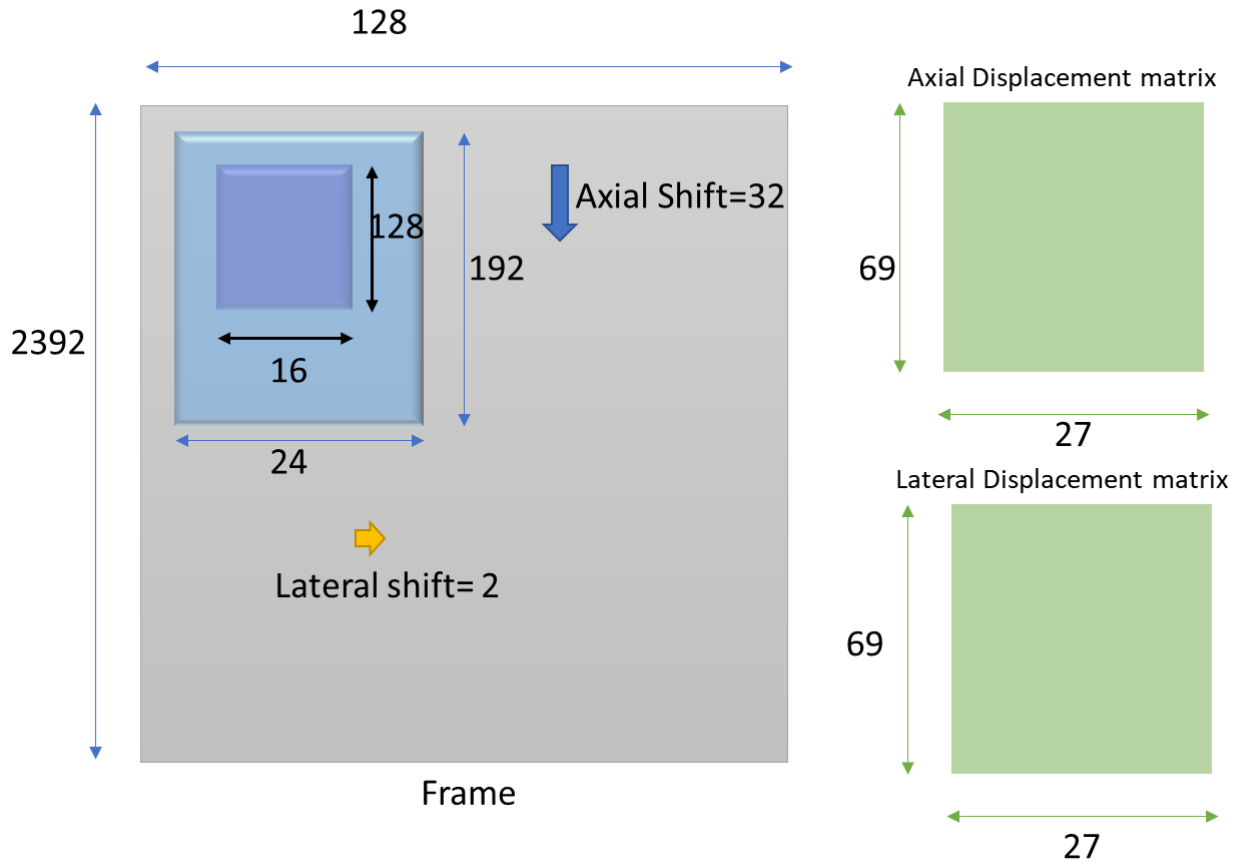


Fig. 3.4 Size comparison in pixels.

Step 2: Displacement Error Correction and Strain Estimation from Displacements

Normalized cross-correlation coefficient was utilized as a confidence metric equivalent to the dependability of the displacement estimate. Displacement estimates having a low normalized cross-correlation coefficient (less than 0.8) were excluded and then interpolated from adjacent displacement estimates that contain a higher normalized cross-correlation value. There were very few inaccuracies in the boundary regions which were also corrected by the surrounding neighbors.

Then the displacement matrices are median filtered to reduce the effect of the shot noise at the cost of some spatial resolution. The median filtering parameter was applied empirically according to the resolution of the displacement estimates. To overcome the major echo-signal decorrelations originating from gradient-based strain computing methods due to the existence of irregular random non axial motion in the case of patient data, least-square estimation was used to compute the strain matrix.

Step 3: Registering Strain to Pre-Compression Frame Size

The strain matrix loses some of its spatial resolutions as least square estimation is used for the computation of the strain matrix from the displacements. This loss is accounted for by registering the locations of the strain points corresponding to the displacement matrix and subsequent bicubic interpolation to fill the in-between missing values. Bi cubic method was used for interpolation as it is computationally faster, and the no of missing values is comparatively low. Then the loss recovered strain matrix is registered to the frame size using spline interpolation by establishing point-to-point correspondence between the strain matrix and pre/post-compression data grid. The interpolation assures a smoothened upscaled strain matrix. On some occasions, there is a need for extrapolation. The extrapolation is implemented in the 2nd iteration based on the interior values after the initial interpolation is completed as depicted in Fig. 3.5.

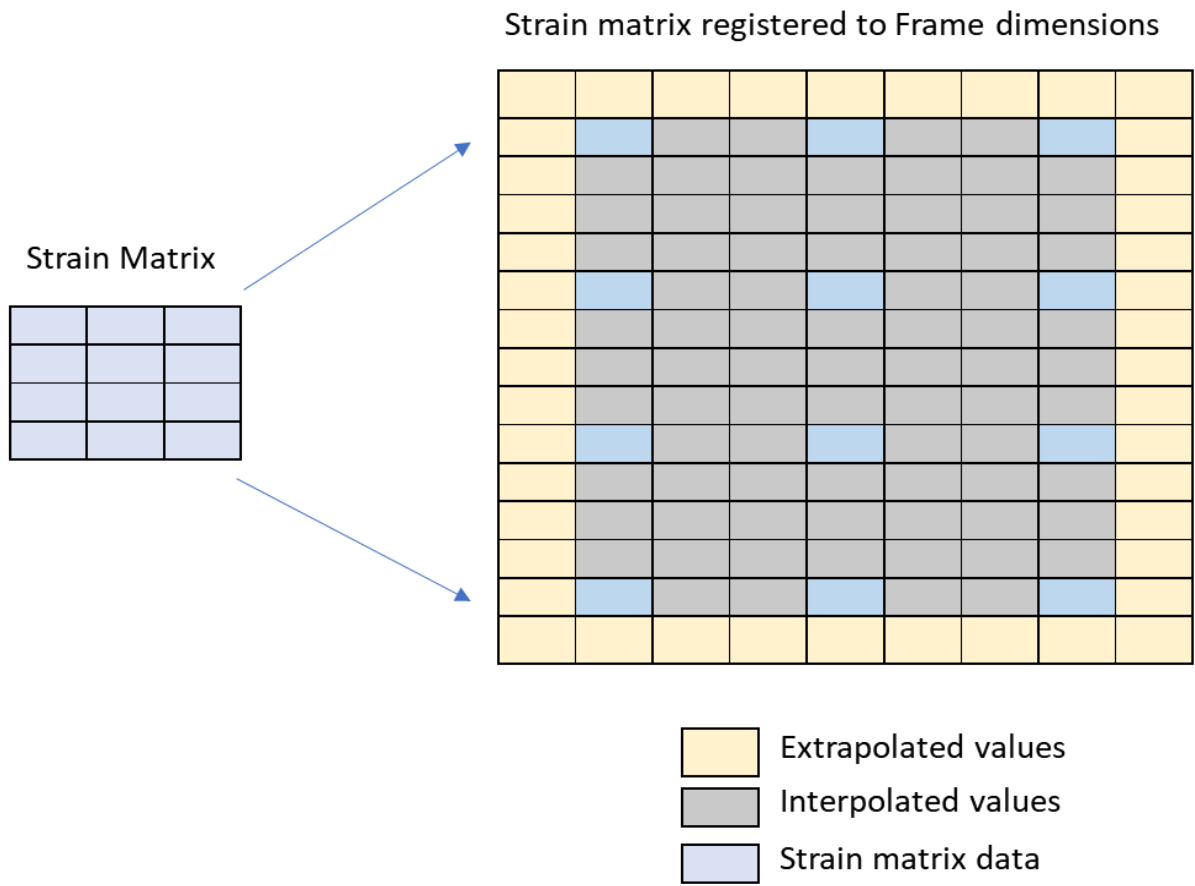


Fig. 3.5 Strain registration with iterative extrapolation.

Bicubic Spline Interpolation

In this section, the theory of bicubic spline interpolation is discussed.

Bicubic interpolation is a two-dimensional cubic interpolation. It is made up of third-order polynomial pieces that are arranged in grid squares [51], [52]. Bicubic spline interpolation gives a third order 2D polynomial to each unit in the data set of four-unit squares patched together similar to Fig. 3.6.

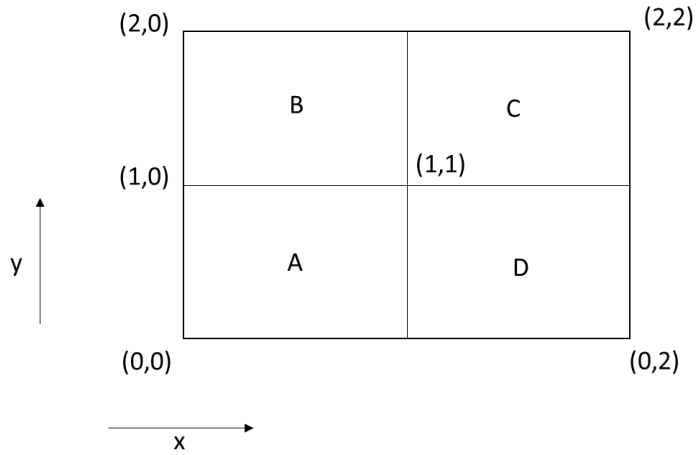


Fig. 3.6 Bicubic interpolation grid.

It is in the form of the equation 3.2 for patch A.

$$f(x, y) = \sum_{i=0}^3 \sum_{j=0}^3 a_{ij} x^i y^j \quad 3.2$$

The partial derivatives can be expressed by

$$\partial_x f(x, y) = \sum_{i=1}^3 \sum_{j=0}^3 i a_{ij} x^{i-1} y^j \quad 3.3$$

$$\partial_y f(x, y) = \sum_{i=0}^3 \sum_{j=1}^3 j a_{ij} x^i y^{j-1} \quad 3.4$$

$$\partial_{xy} f(x, y) = \sum_{i=1}^3 \sum_{j=1}^3 i j a_{ij} x^{i-1} y^{j-1} \quad 3.5$$

Suppose the function values $f(x, y)$, the first derivatives $\partial_x f(x, y)$, $\partial_y f(x, y)$ and, the cross derivatives $\partial_{xy} f(x, y)$ are known at corner knots $(0,0)$, $(1,0)$, $(0,1)$ and $(1,1)$ of the rectangular patch A. Therefore, in order to estimate the unknown coefficients of each polynomial, a total of 16 boundary conditions (equations produced by 3.2-3.5) must be satisfied.

When just the function values, but not the first or cross derivatives, are available various methodologies can be used to calculate these derivatives. The finite difference approach can be used to approximate them according to equations 3.6, 3.7, and 3.8.

$$\partial_x f(x, y) = [f(x + 1, y) - f(x - 1, y)]/2 \quad 3.6$$

$$\partial_y f(x, y) = [f(x, y + 1) - f(x, y - 1)]/2 \quad 3.7$$

$$\partial_{xy} f(x, y) = [f(x + 1, y + 1) - f(x - 1, y) - f(x, y - 1) + f(x, y)]/4 \quad 3.8$$

This method creates a continuous surface patch with first and second derivatives on the unit square having coordinates $(0,0)$, $(1,0)$, $(0,1)$, and $(1,1)$. Thus, the cubic spline interpolation is a better choice of interpolation technique compared to linear or average interpolation for our work.

Step 4: Unwarping Frame 2

Unwarping is used for finding the residual motion that conventional motion algorithms do not take account of. The concept arises from untwisting or reforming after it has been initially twisted or deformed. The post-compression data grid is obtained after the pressure is applied from the transducer. Thus, it had been deformed initially. A method to compensate for the deformation at the pixel level through using the motion estimates from the motion estimation is the main idea of the unwarping procedure.

Considering each displacement pixel to be at the center of the kernel, the axial and lateral displacements are registered to the frame. The missing values in this upscaled displacement matrix are then interpolated using the cubic spline interpolation.

After interpolation, the upscaled displacements were used to unwarp the post-compression RF signal at each pixel through transforming the displacement grid to the post data grid and interpolating the intermediate values through spline interpolation.

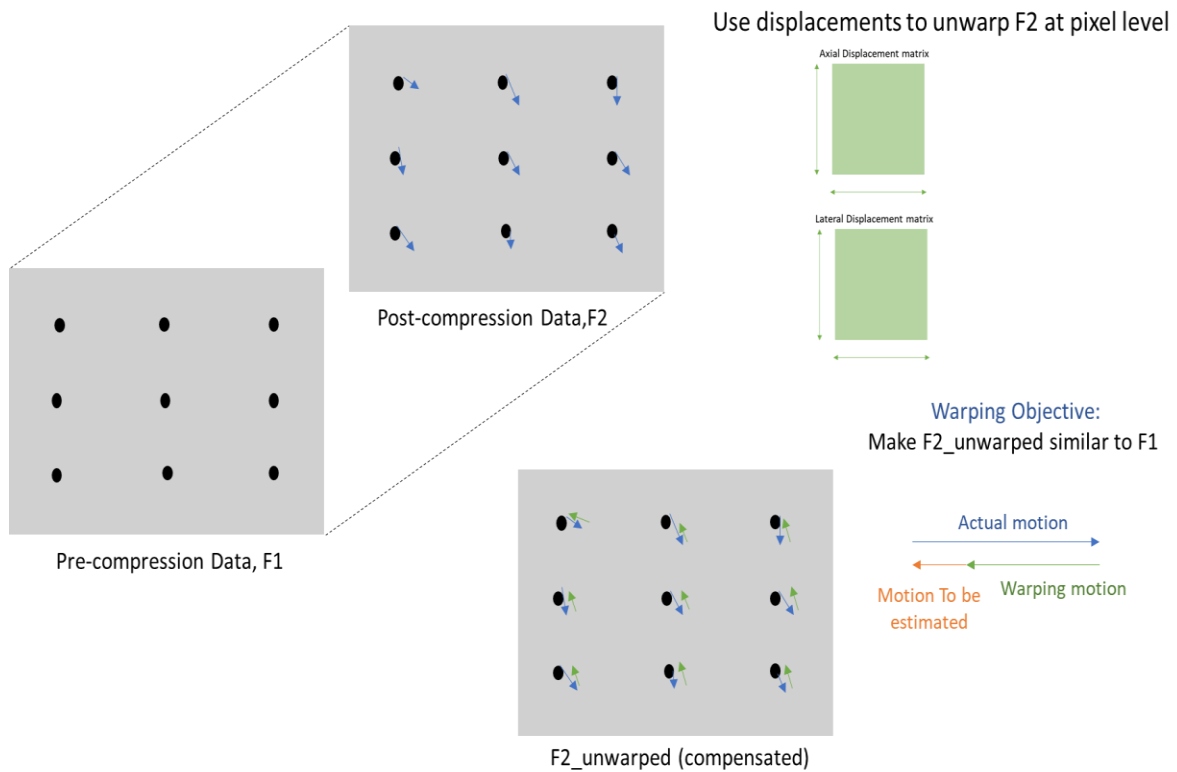


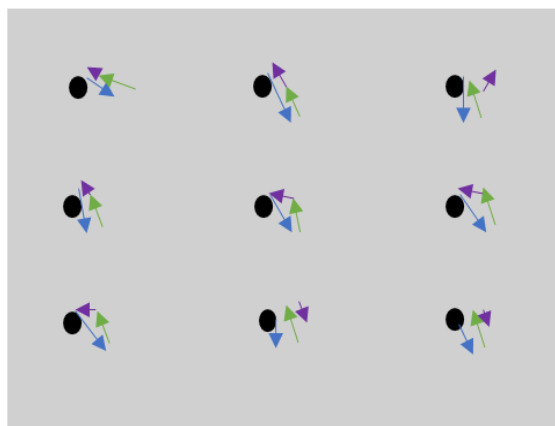
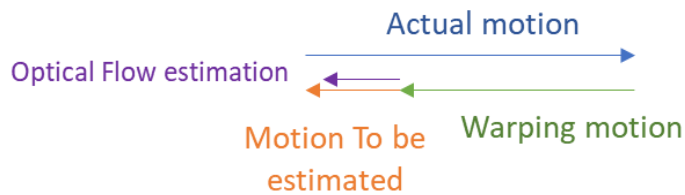
Fig. 3.7 Unwarping frame 2.

The goal of the unwarping in this stage was to make F2 suitable for motion tracking using the subsequent optical flow processing layer. The post-compression data grid is obtained after the pressure is applied from the transducer. The blue arrow shows the actual motion that the tissue has experienced due to the application of force from the transducer. To reverse the experienced motion, F2 was warped such that F2_unwarped is coherent with F1 and meets the optical flow

criteria. This warping motion is shown by the green arrow, and the orange arrow shows the residual motion to be estimated.

Step 5: Optical Flow Between Unwarped Frame 2 And Frame 1:

For estimating the residual motion between F2_unwarped and F1, the optical flow based on the Horn-Shunck method is utilized. The key assumptions for implementing the optical flow method are color constancy and small motion. This implicates that this methodology allows for pixel-to-pixel comparison on a small scale. The Horn-Shunck Optical Flow: method is a global search method that allows smooth flow, i.e., flow can vary from to pixel. Thus, it is suitable for our thesis work as the motion we expect is small, and overall good brightness constancy is maintained. The optical flow method yields a motion vector across both axial and lateral directions. We use the resultant motion field vector combining both the axial and lateral flow fields.



Optical Flow vectors between F2_unwarped and F1

Fig. 3.8 Optical flow between unwarped Frame 2 and Frame 1.

In this step, the optical flow vectors between F2_unwarped and F1 is represented by the purple arrow in Fig. 3.8. The purple arrow is a close approximation of the residual motion that was intended to be estimated at the end of step 4.

Horn-Shunck Optical Flow:

The Horn-Shunck optical flow method [53] is a global minimization problem to compute the motion vectors from the flow field. In this approach, the motion field of images $I(x, y, t)$ and $I(x, y, t')$ is estimated.

For ensuring brightness constancy between the two frames, one can write,

$$I(x + u\delta t, y + v\delta t, t + \delta t) = I(x, y, t) \quad 3.9$$

$$I(x, y, t) + \frac{\partial I}{\partial x} \delta x + \frac{\partial I}{\partial y} \delta y + \frac{\partial I}{\partial t} \delta t = I(x, y, t) \quad 3.10$$

$$\frac{\partial I}{\partial x} \delta x + \frac{\partial I}{\partial y} \delta y + \frac{\partial I}{\partial t} \delta t = 0 \quad 3.11$$

$$I_x u + I_y v + I_t = 0 \quad 3.12$$

where $t + \delta t = t'$; u, v are flow fields along the x and y-directions.

For every pixel, the brightness constancy, E_d can be expressed by

$$E_d(i, j) = [I_x u_{ij} + I_y v_{ij} + I_t]^2 \quad 3.13$$

The smoothness term can be expressed by

$$E_s(i, j) = \frac{1}{4} \left[(u_{ij} - u_{i+1, j})^2 + (u_{ij} - u_{i, j+1})^2 + (v_{ij} - v_{i+1, j})^2 + (v_{ij} - v_{i, j+1})^2 \right] \quad 3.14$$

The Horn Shunck optical flow method considers both brightness constancy and smoothness of the flow field. Thus, the overall objective function for minimization in this algorithm can be expressed as

$$\min_{u,v} \sum_{i,j} \{E(i,j)\} = \min_{u,v} \sum_{i,j} \{E_s(i,j) + \lambda E_d(i,j)\} \quad 3.15$$

Combining equations 3.13 and 3.14 the objective function can be expressed as,

$$E(i,j) = \left\{ \frac{1}{4} \left[(u_{ij} - u_{i+1,j})^2 + (u_{ij} - u_{i,j+1})^2 + (v_{ij} - v_{i+1,j})^2 + (v_{ij} - v_{i,j+1})^2 \right] + \lambda [I_x u_{ij} + I_y v_{ij} + I_t]^2 \right\} \quad 3.16$$

Computing the partial derivatives of the objective function of equation 3.16, the flow field equations for each pixel can be derived. While not converged, updates to the flow fields are computed for each pixel according to equations 3.17 and 3.18.

$$\hat{u}_{kl} = \bar{u}_{kl} - \frac{I_x \bar{u}_{kl} + I_y \bar{v}_{kl} + I_t}{\lambda^{-1} + I_x^2 + I_y^2} I_x \quad 3.17$$

$$\hat{v}_{kl} = \bar{v}_{kl} - \frac{I_x \bar{u}_{kl} + I_y \bar{v}_{kl} + I_t}{\lambda^{-1} + I_x^2 + I_y^2} I_y \quad 3.18$$

where u, v are flow field, I_x, I_y are the precomputed image gradients, I_t is the precomputed temporal gradient.

Finally, the resultant optical flow field is expressed in equation 3.19

$$r = \sqrt{u^2 + v^2} \quad 3.19$$

Step 6: Strain Estimation from Optical Flow Estimates:

In this step, the strain contribution from the residual displacements is taken into account. To overcome the noise associated with a lot of sparse data arising from the conventional gradient-based strain estimation approach, we apply the gradient of the smoothing spline applied initially on the optical flow vectors. Mathematically the smoothing function can be represented by equation 3.20.

$$s \sum_i [y(x_i) - \hat{y}(x_i)]^2 + (1 - s) \int \left(\frac{d^2 \hat{y}}{dx^2} \right)^2 dx \quad 3.20$$

where $s = (0 \leq s \leq 1)$ represents smoothing parameter and \hat{y} is a piecewise cubic polynomial that can be differentiated three times. The gradient of the smoothing-spline \hat{y} is used to calculate strain.

This assures smoothening of the optical flow strain field and makes it usable for addition with the strain map from block matching.

Step 7: Stage 1 Strain Estimation

In this stage, the strain from optical flow and motion estimation are added together. A gaussian smoothening filter is then applied to remove shot noises and reduce the jaggy effect inherent to optical flow strain vectors.

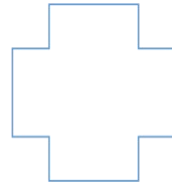
The gaussian smoothening filter can be mathematically expressed as

$$G(x, y) = \frac{1}{2\pi\sigma^2} e^{-\frac{x^2+y^2}{2\sigma^2}} \quad 3.21$$

Where σ is the standard deviation.



Strain from Optical Flow Stage 1



Strain from Block matching



Stage 1 Strain

Fig. 3.9 Strain estimation at stage 1.

3.3.2 Stage 2: Introducing the Third Frame in The Algorithm

This is stage 2 of the algorithm, where the third frame in the algorithm is introduced. The addition of this stage is to increase the accuracy and precision of the strain estimation from stage 1. This stage finalizes and improves the accuracy of the displacement estimation of stage 1 by trying to estimate residual flows that stage 1 does not take account of.

Step 8: Choosing Frame 3 Slightly After Frame 2

Under the application of the stress, another post-compression frame, F3, is then selected after a smaller time interval of δt , i.e., after the selection of F2. Most of the deformation generally occurs before time $(t + \Delta t)$, i.e., at the onset of selecting F2 as the clinician stops implying more force at a certain stage. Thus, the deformation between F2 and F3 is less compared to that between F1 and F2. The nature of this data acquisition is exploited in this stage of the algorithm.

Step 9: Warping Frame 2

This concept of warping is like unwarping, which can be defined as untwisting or reforming after it has been initially twisted or deformed. For warping, the motion anticipated is added instead of untwisting. The post-compression data grid is obtained after the force is applied from the transducer. A method to estimate the deformation after a certain interval from the previous post-compression data to reconstruct a new post-compression data at the pixel level like post-compression frame 3 through using the motion estimates from the motion estimation is the main idea of the warping procedure.

Considering each displacement pixel to be at the center of the kernel, the axial and lateral displacements are registered to the frame. The missing values in this upscaled displacement matrix are then interpolated using the cubic spline interpolation.

After interpolation, the upscaled displacements are used to warp the post-compression B-mode signal F2 at each pixel through transforming the displacement grid to the post-data grid and interpolating the intermediate values through spline interpolation. After this operation, we get warped frame F2.

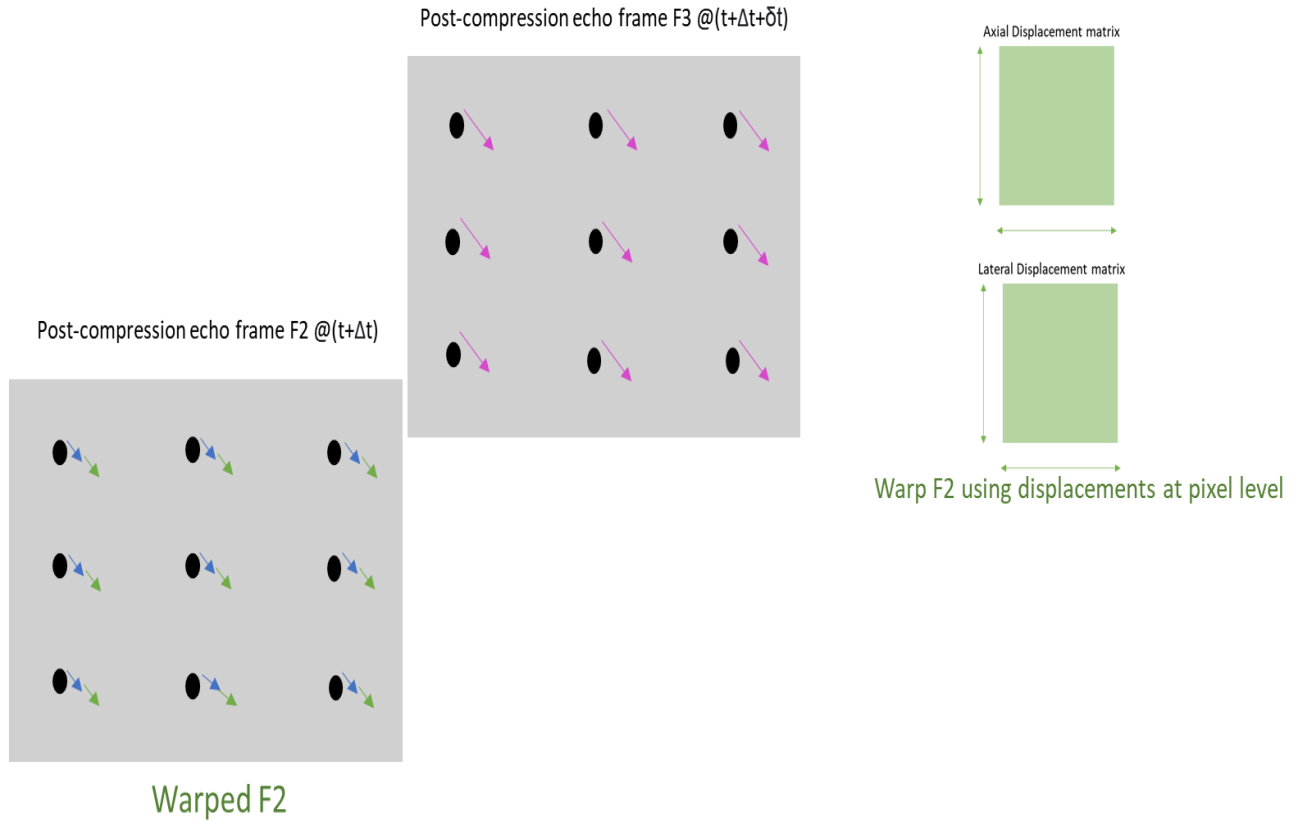


Fig. 3.10 Warping post-compression frame F2.

Step 10: Finer Displacement Estimation Between Warped Frame 2 And Frame 3 Through Optical Flow

The warping in the previous step allows for finer displacement estimation. The warping reconstructs a new post-compression data, which is a closer approximation to the post-compression frame F3. For estimating motion between F2_warped and F3, the optical flow based on the Horn-Shunck method is applied. The preconditions for implementing Horn-Shunck based optical flow method are color constancy and small motion. These conditions are met by implementing the previous step. Thus, pixel-to-pixel comparison between the

reconstructed frame and F3 is possible on a small scale. Thus, we estimate the finer motion between F2_warped and F3 by the Horn-Shunck method illustrated in Fig. 3.11.

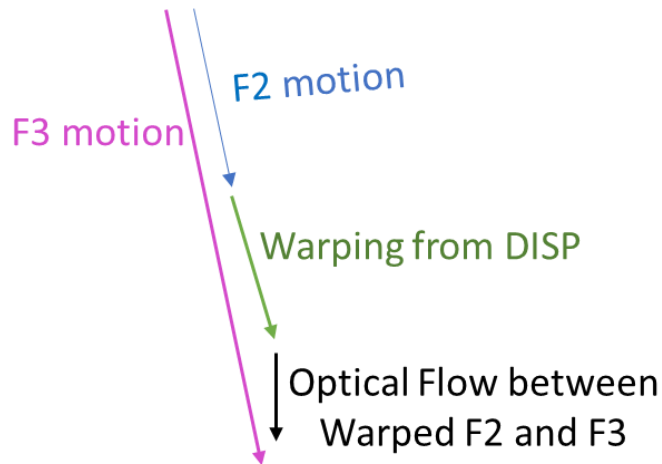


Fig. 3.11 Finer displacement estimation between warped frame 2 and frame 3.

Step 11: Strain Estimation from Optical Flow Vectors

In this step, the strain contribution from the optical flow between Warped F2 and F3 are estimated. To estimate the strain contribution, we take gradients after applying the smoothing similar to stage 1, i.e., equation 3.20. This assures smoothing of the optical flow strain field. This strain field contains some noise. A gaussian smoothing filter like equation 3.21 is applied in addition to median filtering to eliminate the jaggy nature of noise arising from pixel-based motion estimation of optical flow.

Step 12: Final Strain Estimation:

In this stage, the strains from all the strains of different stages are added after registering them to the frame dimensions to create the final strain image. After the generation of the final strain image, post-processing filters like median filters and gaussian smoothing windows are applied in small patches. This marks the end of the optical flow based multi-frame (OFMF) strain estimator.

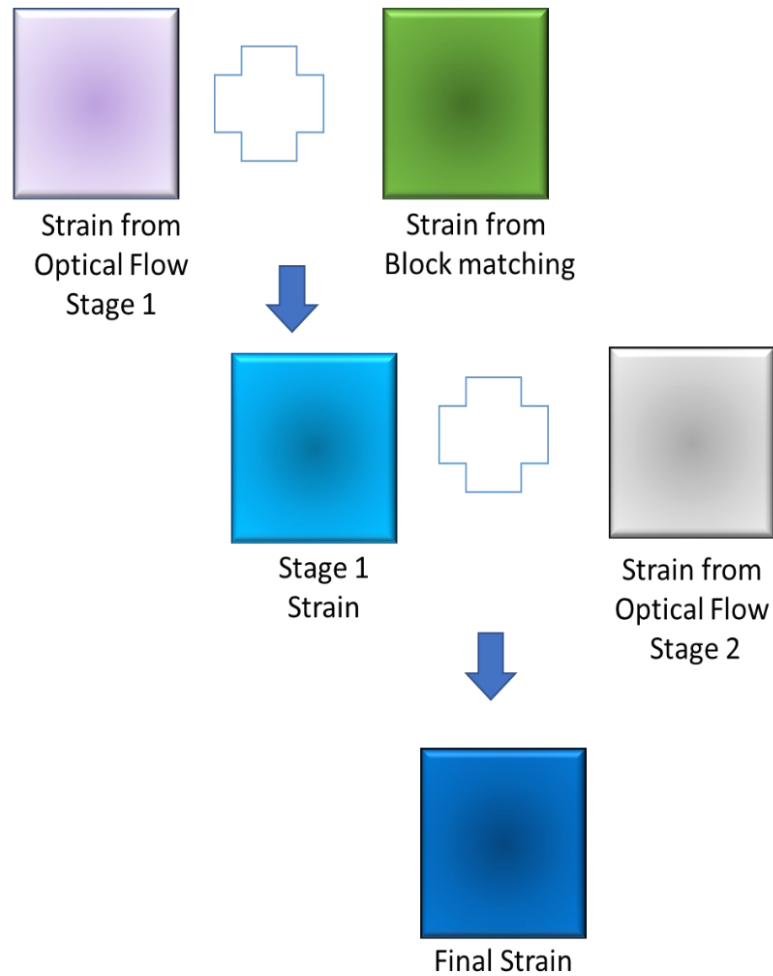


Fig. 3.12 Final strain estimation of optical flow-based multi-frame (OFMF) strain estimator.

The workflow of this algorithm can be summarized in the flowchart of Fig. 3.13.

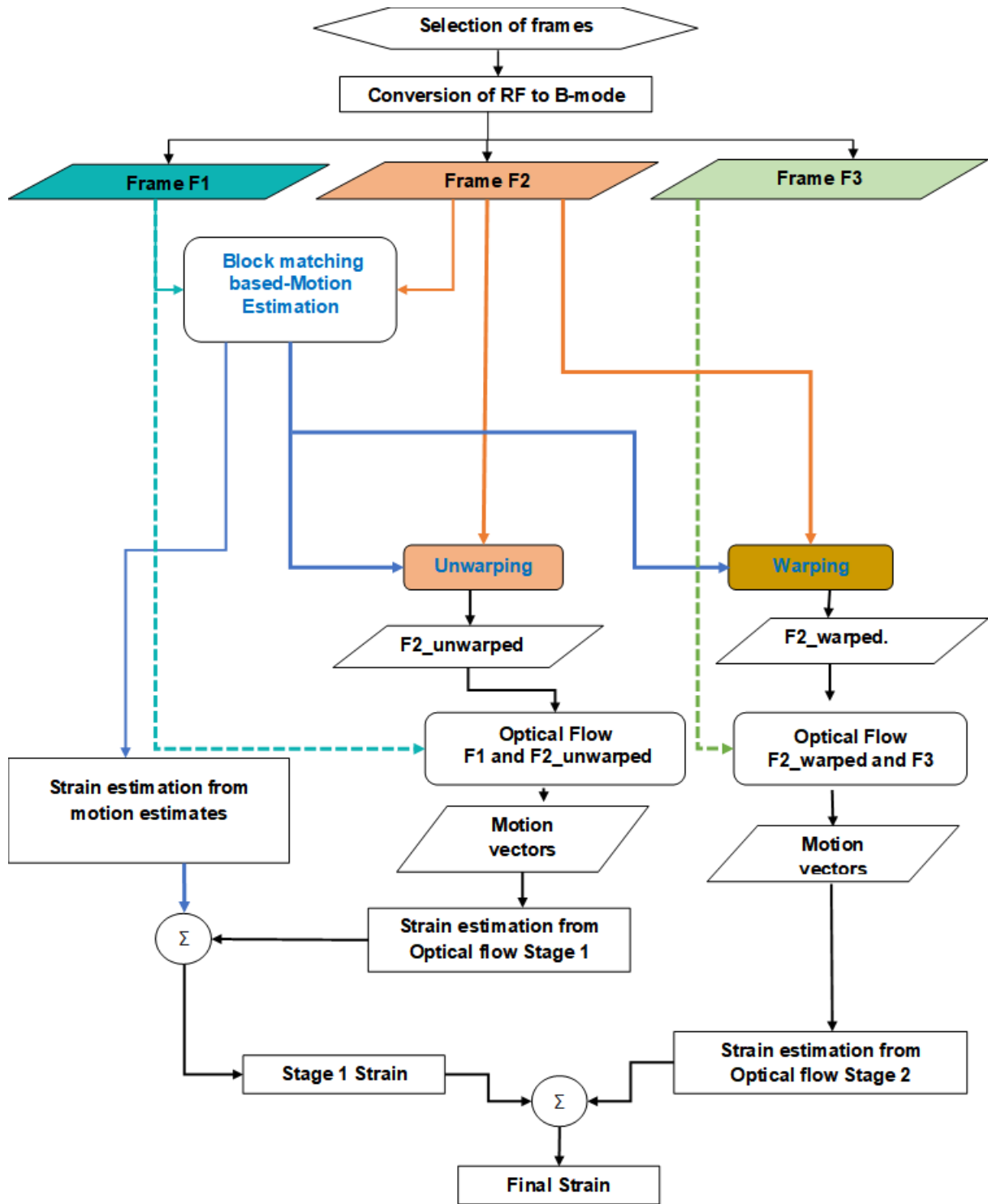


Fig. 3.13 Flowchart of optical flow-based multi-frame (OFMF) strain estimator.

3.4 Multistage Optical Flow-Based Multi-Frame Strain Estimator

The optical flow-based multi-frame (OFMF) strain estimator can be improved even further if the motion estimation of stage 1 step 1 can be performed even more precisely. For the improvement of this algorithm, the multistage motion estimation and subsequent multistage strain registration were integrated into the previous algorithm.

3.4.1 Multistage Motion Estimation

Like the earlier algorithm, we chose 2D normalized cross-correlation to maximize the cost function. Sizes of kernel and search-window were carefully selected to maximize the cross-correlation function and thus have less impact on signal decorrelation. The corresponding displacement to this maximum similarity gives the crude peak displacements. Thus, sliding the kernels and search windows at a certain degree of overlap with pre-defined axial and lateral shifts, the initial displacement matrices are obtained. These matrices account for both the axial and lateral displacements of the initial stage obtained from the B-mode of the pre- and post-compression echo signal.

Mathematically the cross-correlation function in this stage can be represented by equation 3.1

Typical multilevel hierarchical block-matching algorithms estimate motion in a coarse resolution down-sampled image pair initially, then refine the initial response in finer resolutions within a limited search range. The downsampling leads to the loss of intricate information that cannot be retrieved in the final stages as the motion is not coherent in a larger ROI. This might lead to erroneous displacement estimation if the coarse level displacements are qualitatively bad.

Scaling down the size of the kernel and the search window without altering the image pair reduces the decorrelation noise. However, in order to detect the finer displacements, the block matching is initiated after the search window is repositioned utilizing the initial stage coarse

displacements to ensure the confinement of the tracked tissue within the search window with a restricted range to minimize false peak error as far as possible. This can be analogized to zooming into the solution.

This is implemented according to the steps below:

- Initial stage coarse displacements are mapped into a grid that replicates the dimensions of the next stage displacement matrices (larger) utilizing cubic-spline interpolation. This interpolated grid is the reference displacement or initial condition for the subsequent stage.
- The search window is then repositioned using the reference displacement matrices, and then block matching is reiterated with the scaled-down kernel, search window, and window shift sizes.

During reiteration of block matching, the cross-correlation function can be denoted by the following

$$\begin{aligned}
 & NCC(i, j) \\
 &= \frac{\sum_{x=1}^M \sum_{y=1}^N [f(x, y) - \bar{f}] [t(x + i + i_0, y + j + j_0) - \bar{t}]}{\sqrt{\sum_{x=1}^M \sum_{y=1}^N [f(x, y) - \bar{f}]^2 * \sum_{x=1}^M \sum_{y=1}^N [t(x + i + i_0, y + j + j_0) - \bar{t}]^2}} \quad 3.22
 \end{aligned}$$

where f and t represent the pre- and post-compression data frames. i and j denote relative shifts between the f and t data frames, i_0 and j_0 represent the shift between f and t in the reference displacement grid in the x and y directions respectively, M and N are the block sizes in axial and lateral directions, where \bar{f} and \bar{t} denote the mean values of the intensities of the blocks f and t used in the calculation.

This repositioned iteration of block matching steps not only ensures the data is tracked precisely but also makes the algorithm suitable for multiresolution strain mapping at the end by generating higher resolution displacement maps.

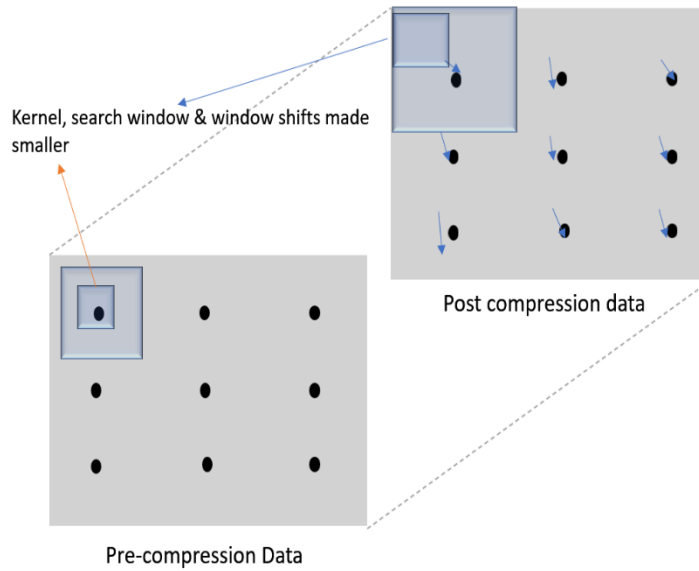


Fig. 3.15 Motion estimation after repositioning search window - $x1'$ and $y1'$ represent reference lateral and axial displacements from previous stage respectively; $X1$ and $Y1$ represent lateral and axial displacement to be estimated in current stage respectively.

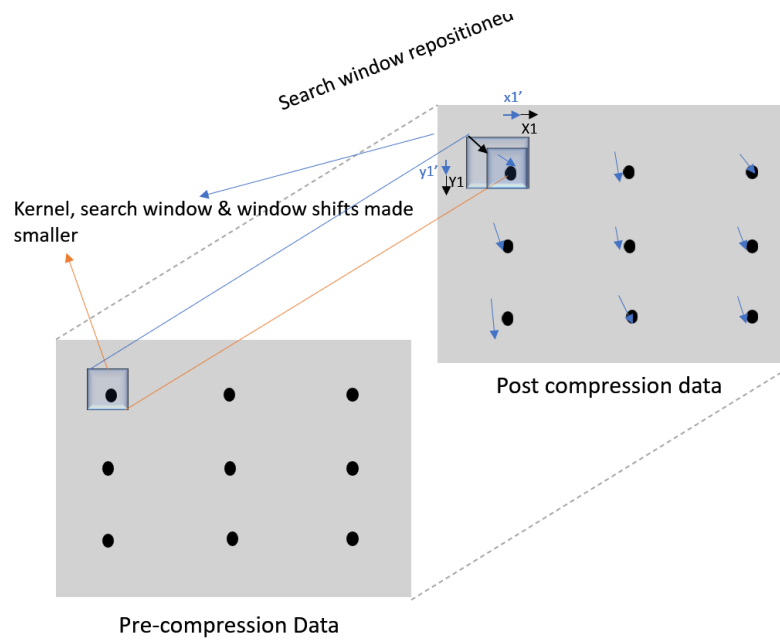


Fig. 3.14 Scaling down processing parameters before repositioning.

In all the stages, the normalized cross-correlation coefficient was utilized as a confidence metric equivalent to the dependability of the displacement estimate. Displacement estimates having a low normalized cross-correlation coefficient (less than 0.8) were excluded and then interpolated from adjacent displacement estimates that contain a higher normalized cross-correlation value. There were very few inaccuracies in the boundary regions, which were also corrected by the surrounding neighbors.

Subpixel displacement estimation was incorporated in the last stage of the multistage estimation to improve the precision of the displacement estimates considering the displacements have irregular time shifts due to imprecision or inaccuracies in the transducer. This estimates the peak of the sampled crude displacements using 2-D parabolic interpolation.

The vector summation of the multistage procedure in a grid equivalent to dimensions of the last stage displacements gives the true final stage displacements. This can be represented by

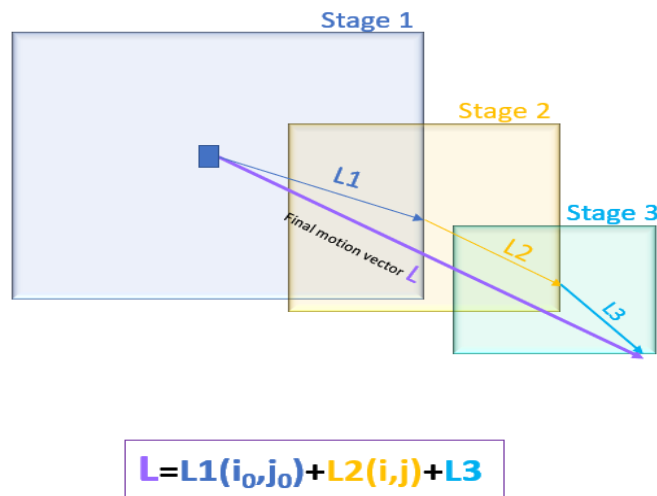


Fig. 3.16.

Fig. 3.16 Vector summation of the multistage displacements

Then the displacement matrices are median filtered to reduce the effect of the shot noise at the cost of some spatial resolution. The median filtering parameter was applied empirically according to the resolution of the displacement estimates corresponding to the different stages in the method.

This final displacement is then used in the earlier algorithm for better results. The flow chart multistage motion estimation is shown in Fig. 3.17.

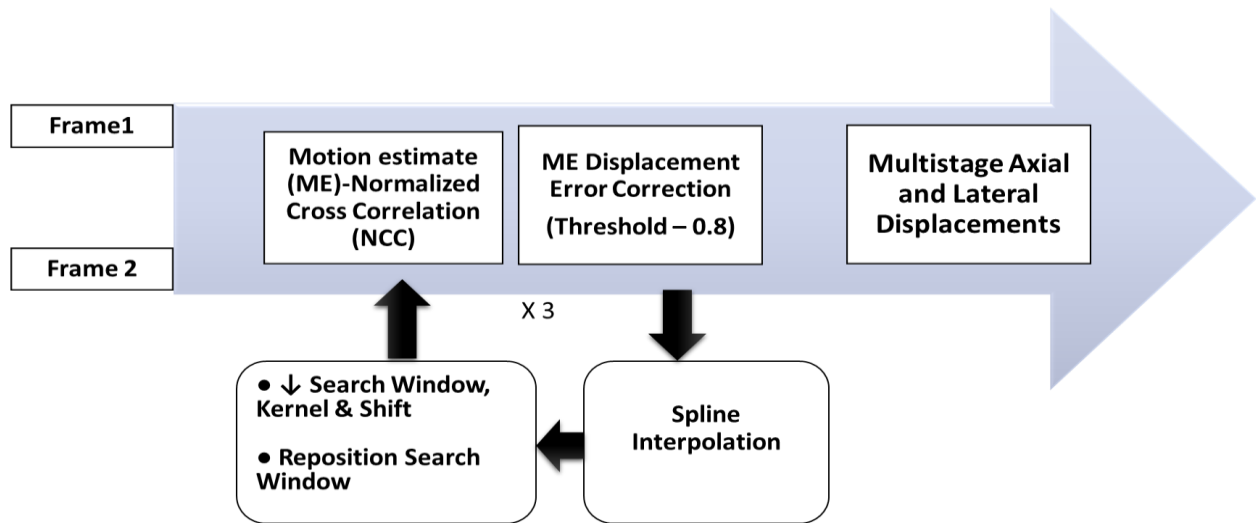


Fig. 3.17 Flow of the multistage motion estimation

3.4.2 Multistage Strain Estimation and Registration

To overcome the major echo-signal decorrelations originating from gradient based strain computing methods due to the existence of irregular random non axial motion in case of patient data, least square estimation was used to compute the strain matrices corresponding to the displacements at each stage.

Image registration is widely used for transforming different sets of data into one coordinate system. A high-resolution image is generated by combining the indispensable information contained in multiple low-resolution images. Thus, image registration techniques involve spatially transforming the source image(s), i.e., low-resolution ones, to align with the target image high resolution one. In our algorithm, the source data are the gradual resolution

increasing strain images of the processing stages, i.e., the strain images of the 1st to 4th stage. The selection of the target image or the final image is generally based on the known correspondences between source and target image. In this algorithm, the processing parameters (the kernel, search window and shift sizes) are used as the correspondence parameter between the source and initial pre-compression grid. Since a relationship between the strain matrices and the initial pre-compression data can be established, the pre-compression grid was selected as the target image in our case.

The strain images of all the stages, i.e., source images, are mapped in a pre-compression data equivalent grid, i.e., target image, through the known correspondences. The data in between each corresponding point was bicubically interpolated. It may be claimed that bicubic interpolation has a jaggy or blurred effect on the registered strain images. This effect is nullified by the different spatial positions of the real data points from each stage at the target grid. This can be explained by Fig. 3.18.

Gradually increasing weighted average parameters of the corresponding registered strain images were chosen to emphasize the clarity of edges of the ROI and reduction of noise outside ROI due to the processing. The averaging of the registered strain images ensures that all the prominent features of each corresponding stage are considered.

This registered strain image is used with our earlier algorithm to improve the quality of elastograms at the cost of more complexity. The flowchart depicted in Fig. 3.19 is a summary of the multistage optical flow-based multi-frame (MSOFMF) strain estimator algorithm.

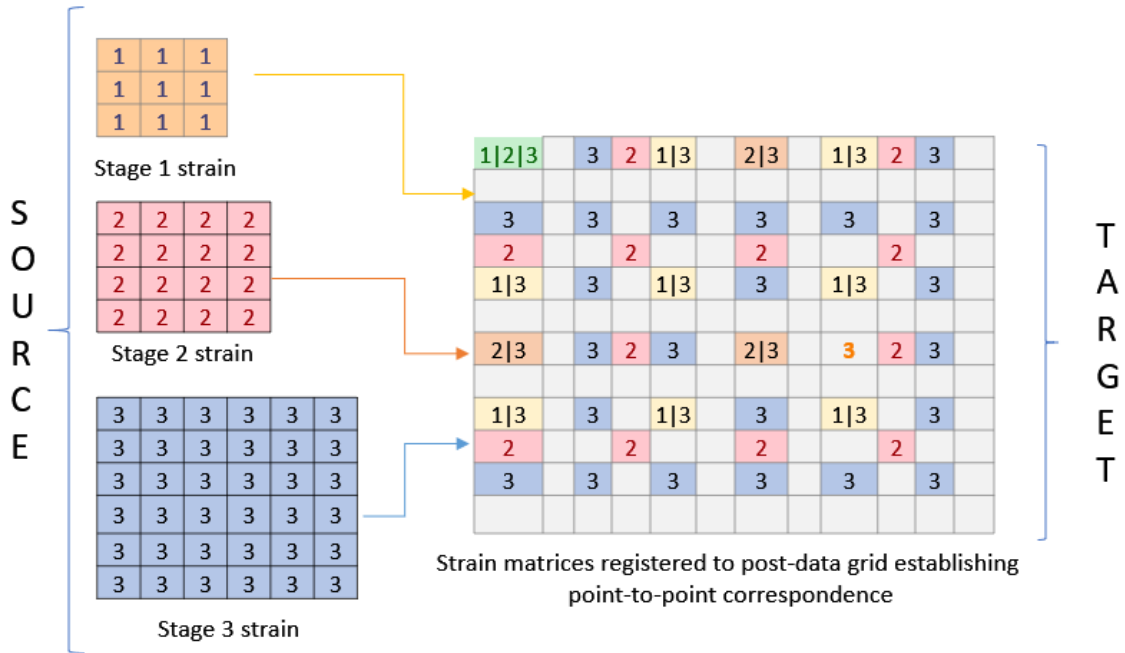


Fig. 3.18 Registration of multistage strain matrices to frame.

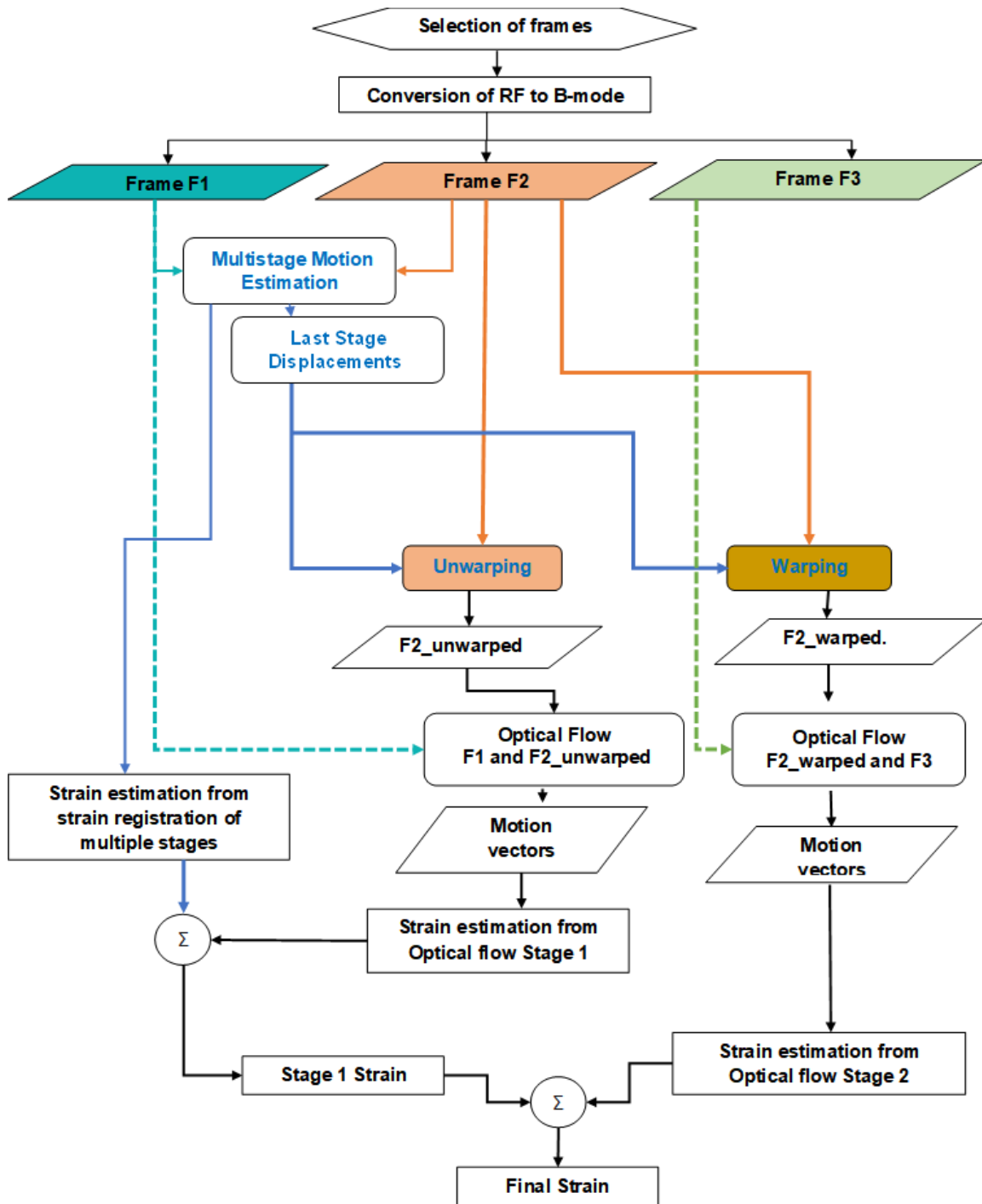


Fig. 3.19 Flowchart of multi-stage optical flow-based multi-frame (MSOFMF) strain estimator

Chapter 4

RESULTS

In this thesis, the results obtained for simulation and in-vivo data (patient data) for both the proposed techniques are first presented. Then the results of the proposed techniques are compared with some well-known algorithms like adaptive stretching, 1D Least square estimator, 2D least square estimator with temporal stretching. Besides subjective evaluation by visual inspection, performances of the above-mentioned techniques in terms of SNR and CNR are compared and analyzed.

4.1 Finite Element Simulation

The performance of the proposed algorithms is tested by using two data sets, one generated artificially using a phantom and the other is patient data sets. Using the analytical program Algor, a rectangular 40 x 40 mm FEM phantom with a total of 30,372 nodes was simulated (Algor Inc). Because the simulation was done using a 2-D Finite Element Method (FEM) model, the out-of-plane motion was not taken into consideration.

This phantom had a uniform backdrop of 60 kPa stiffness with four distinctly stiff circular inclusions of 7.5 mm diameter. The bottom left inclusion was 10 decibels stiffer than the backdrop; the top inclusion was 20 decibels stiffer; the bottom right inclusion was 30 decibels stiffer, and the center inclusion was 40 decibels stiffer. Ensuring free-slip condition at top and bottom surfaces the phantom was compressed from the top using a larger-width planar compressor after being put on a level surface. An ultrasonic transducer with a central frequency of 5 MHz and a bandwidth of 60% was used to scan the phantom from the top with a non-diffracting beam of width of 1.5 mm. In this instance, there were a total of 128 A-lines. The data was up sampled 1.5 times to get 4000 pixels axially and to 196 A-lines laterally. With the addition of zero-mean white noise, the phantom was reproduced beginning at 2% applied strain and increasing to 16% applied strain. Fig. 4.1 depicts the stiffness of the inclusions in the FEM simulation.

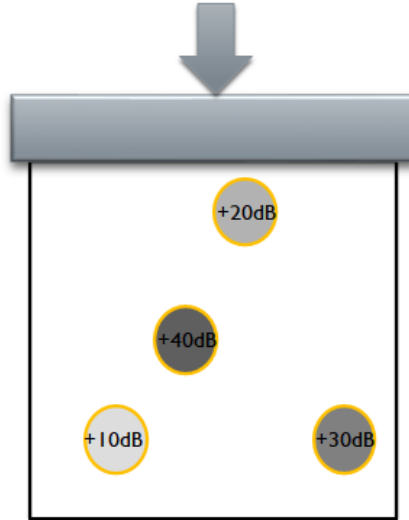


Fig. 4.1 Ideal elastogram from finite element simulation.

4.1.1 Processing Parameters

The processing parameters in case of the simulation data can be summarized in Table 4.1.

Table 4.1 Processing parameters for finite element simulation.

	1 st stage	2 nd stage	3 rd stage
Kernel	256 x 16	128 x 16	64 x 8
Search Window	384 x 24	192 x 24	86 x 16
Shift	32 x 2	24 x 2	20 x 2
Lag restriction	–	±10 x ±2	±4 x ±2

Three stages of motion tracking were used as it provided optimal range of search. Involving more stages worsen the normalized cross-correlation maximums since the kernel does not encompass sizeable amount of data to be tracked with confidence. This can be illustrated with the surf plots of maximum NCC maps of 3rd stage and 4th stage in the Fig. 4.2. As the processing parameters reduce in the higher stage, the maximum NCC coefficients suffer. For instance, if 4th stage with kernel size 32*6, search window of 44*8 and shift of 12*1 are used after the 3rd stage, in the case of the simulation data the mean of the NCC coefficient reduce from 0.94 to

0.82. Thus, in order to mitigate bad motion tracking, motion estimation is stopped at stage 3 to achieve an optimal performance without adding more computation.

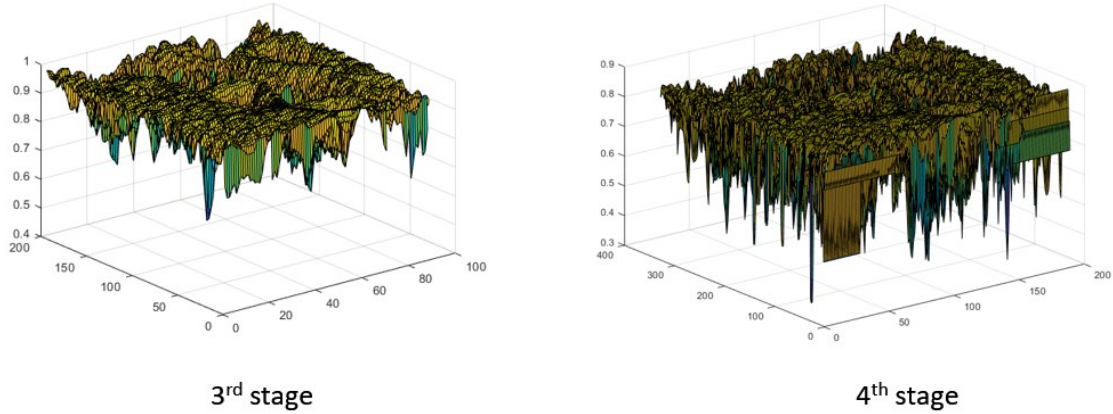


Fig. 4.2 Maximum NCC maps at 3rd stage and 4th stage.

4.1.2 Strain Images

In this simulation, the phantom was produced beginning at 2% applied strain and increasing to 16% applied strain. We implemented both our techniques on these varied applied compressions. In Fig. 4.3, we show the strain images generated by our first proposed technique, “Optical flow-based multi-frame (OFMF)” strain estimator.

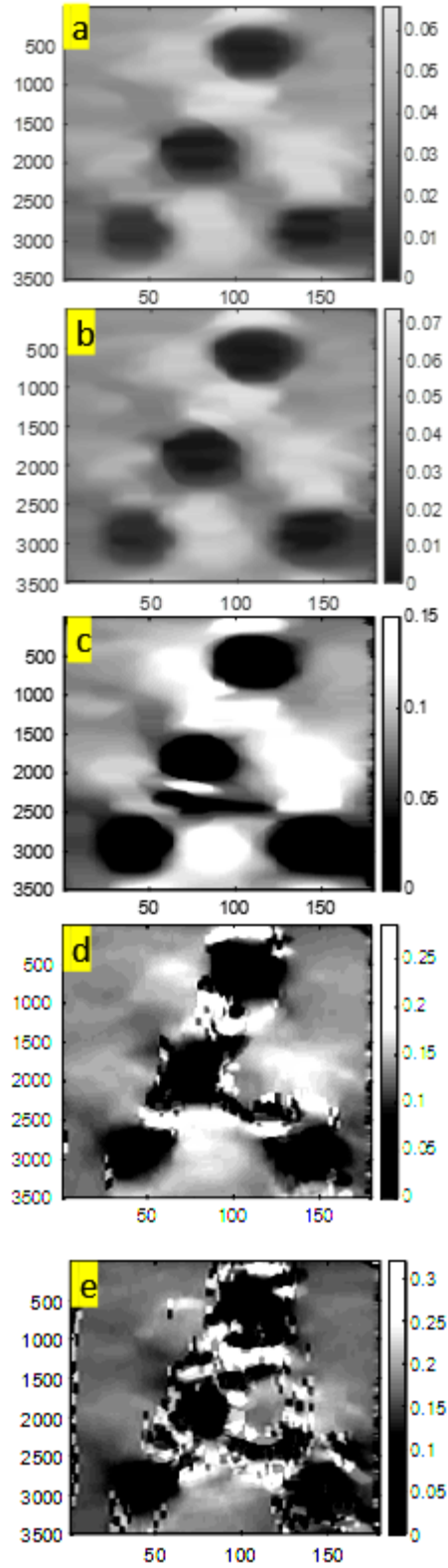


Fig. 4.3 Strain Images of Optical flow-based Multi-Frame (OFMF) Strain Estimator at (a) 2% (b)4% (c) 8% (d) 12% (e) 16% applied strain.

Fig. 4.4 depicts the strain image generated by our second proposed technique, Multistage Optical flow-based multi-frame (MSOFMF) strain estimator.

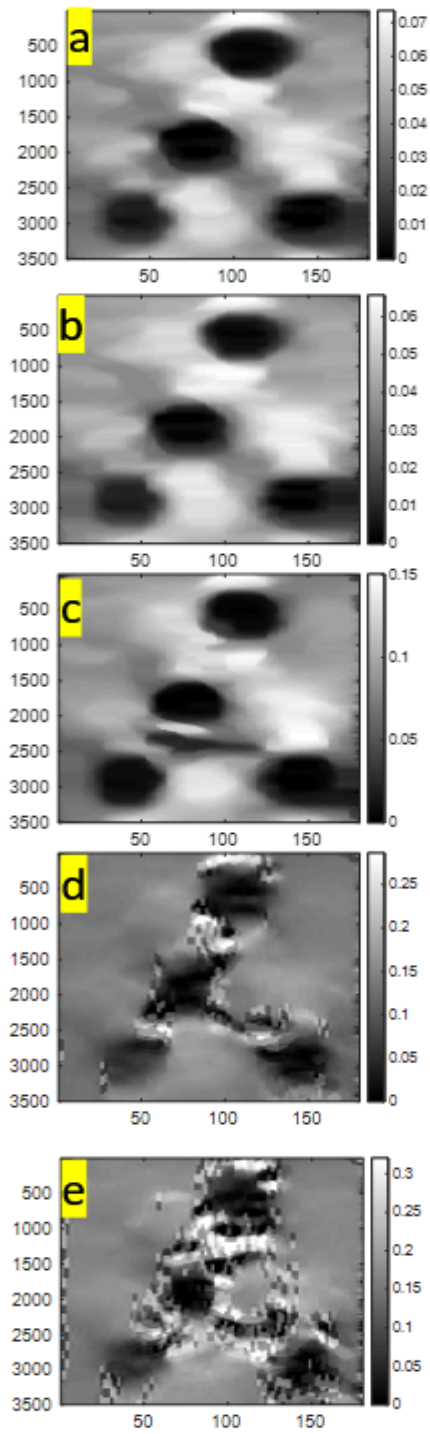


Fig. 4.4 Strain Images of Multistage Optical Flow based Multi Frame (MSOFMF) Strain Estimator at (a) 2% (b)4% (c) 8% (d) 12% (e) 16% applied strain.

Fig. 4.5 gives a visual comparison of our 2nd technique (MSOFMF) strain estimator to other well-established strain estimators like adaptive stretching estimator (1D AS), 1D Least square estimator with uniform stretching (1D LSUS), 2D least square estimator with temporal stretching (2D LSUS).

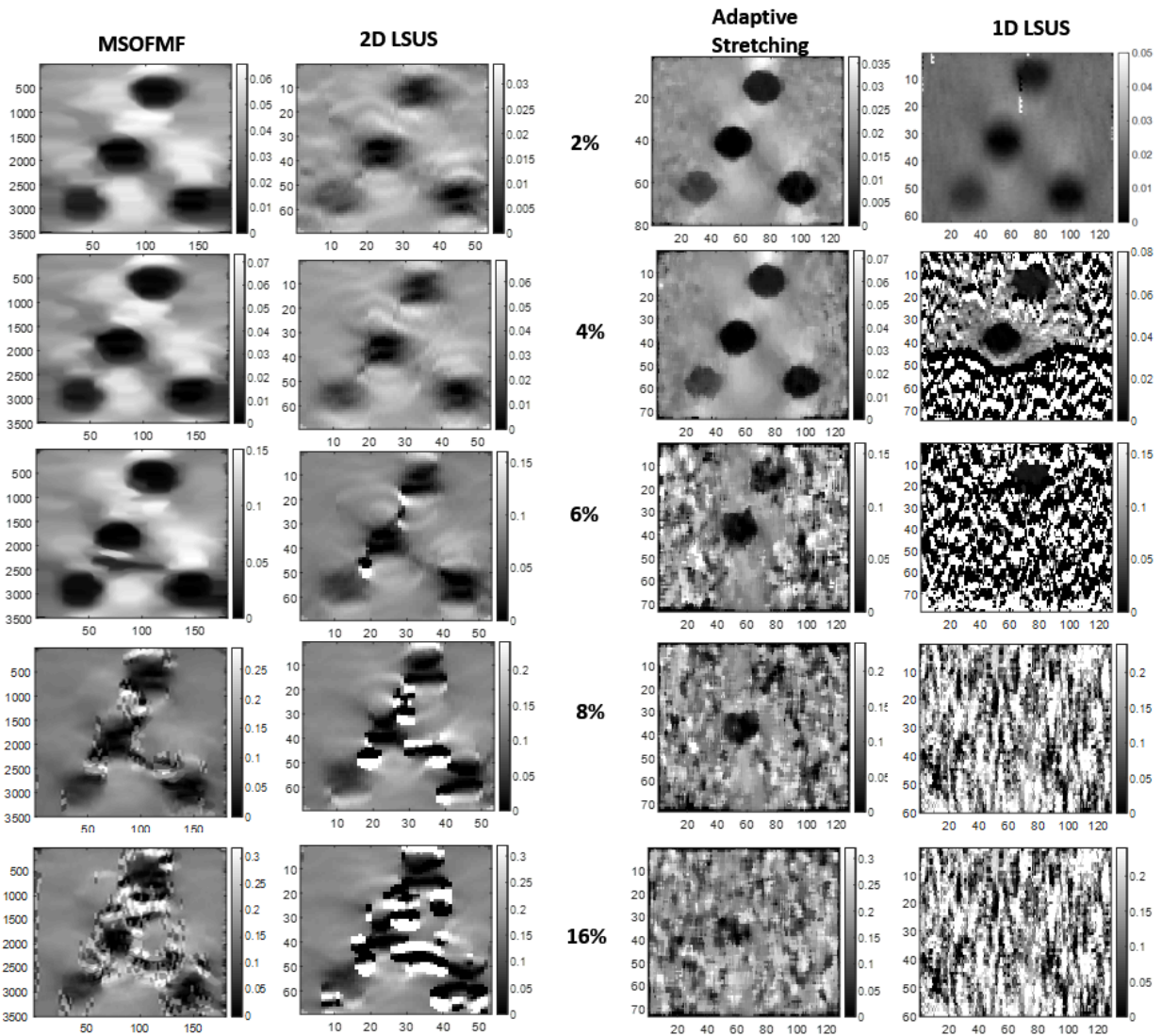


Fig. 4.5 Strain images comparison of various algorithms

4.1.3 Performance Indices

In this work, two performance parameters i.e., SNR and CNR are measured. These quantitatively compare the performance of different strain estimators.

4.1.3.1 Signal to Noise Ratio

The noise level in a strain picture is measured by the SNR, which is specified as [54].

$$\text{SNR} = \frac{\mu}{\sigma} \quad 4.1$$

where the statistical mean and standard deviation of the strain calculated in a homogeneous region are denoted by μ and σ , respectively.

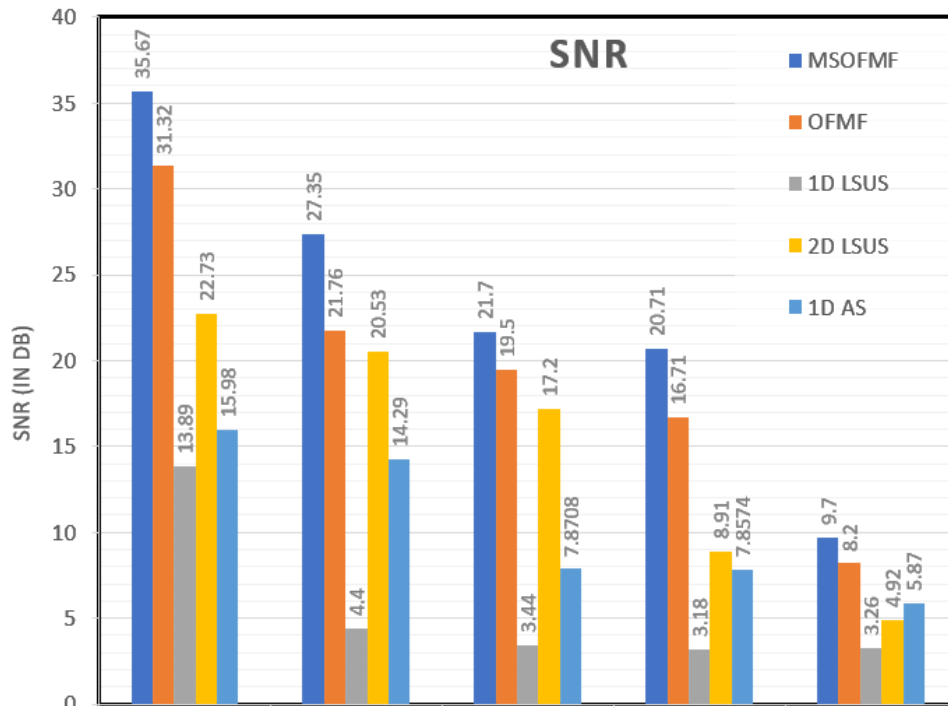


Fig. 4.6 SNR comparison between various strain estimators.

The SNR comparison of the strain estimators discussed above are illustrated in Fig. 4.6 and Table 4.2.

Table 4.2 SNR comparison between various strain estimators.

	2% applied strain	4% applied strain	8% applied strain	12% applied strain	16% applied strain
MSOFMF	35.67	27.35	21.7	20.71	9.7
OFMF	31.32	21.76	19.5	16.71	8.2
1D LSUS	13.89	4.4	3.44	3.18	3.26
2D LSUS	22.73	20.53	17.2	8.91	4.92
1D AS	15.98	14.29	7.8708	7.8574	5.87

4.1.3.2 Contrast to Noise Ratio

The CNR assesses the contrast attributes of a strain picture and is characterized by

$$\text{CNR} = \frac{2(\mu_l - \mu_b)^2}{\sigma_l^2 + \sigma_b^2} \quad 4.2$$

where μ is the mean strain of the image and σ denotes the standard deviation of the strain in a homogeneous area, and the sub subscripts l and b refer to the lesion and the background, respectively.

CNR of the four lesions found by previous algorithms can be presented in the following.

4.1.3.2.1 Top Inclusion

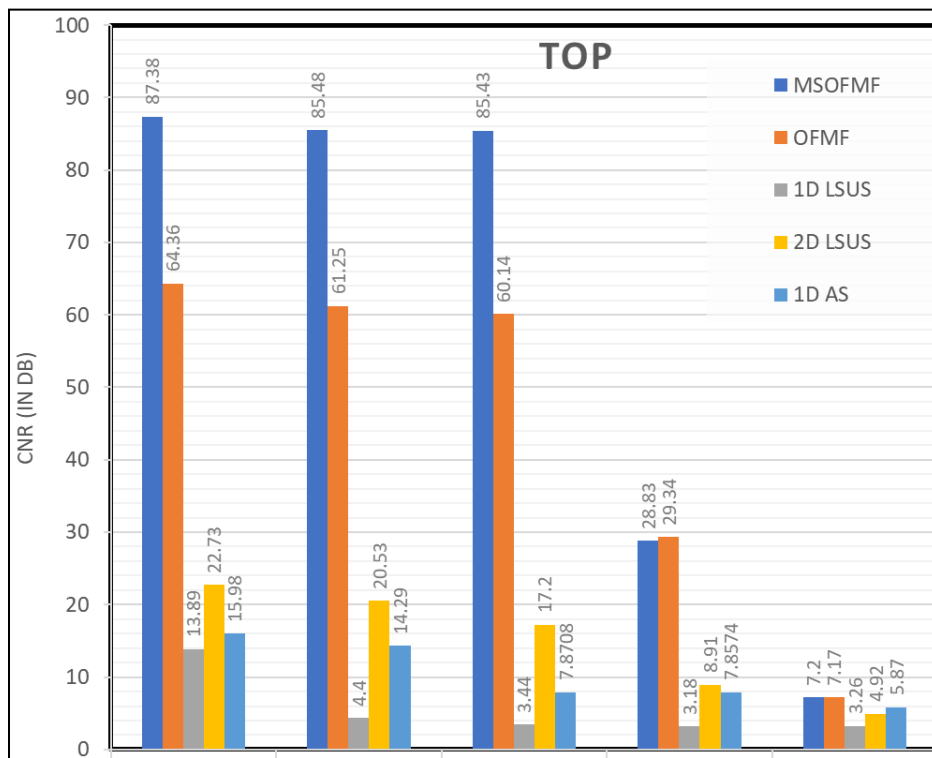


Fig. 4.7 CNR comparison of the top lesion.

shows the different values of the CNR found out by the aforementioned algorithms for the top lesion

Table 4.3 CNR comparison of the top lesion.

	2% applied strain	4% applied strain	8% applied strain	12% applied strain	16% applied strain
MSOFMF	87.38	85.48	85.43	28.83	7.2
OFMF	64.36	61.25	60.14	29.34	7.17
1D LSUS	13.89	4.4	3.44	3.18	3.26
2D LSUS	22.73	20.53	17.2	8.91	4.92
1D AS	15.98	14.29	7.8708	7.8574	5.87

4.1.3.2.2 Centre Inclusion

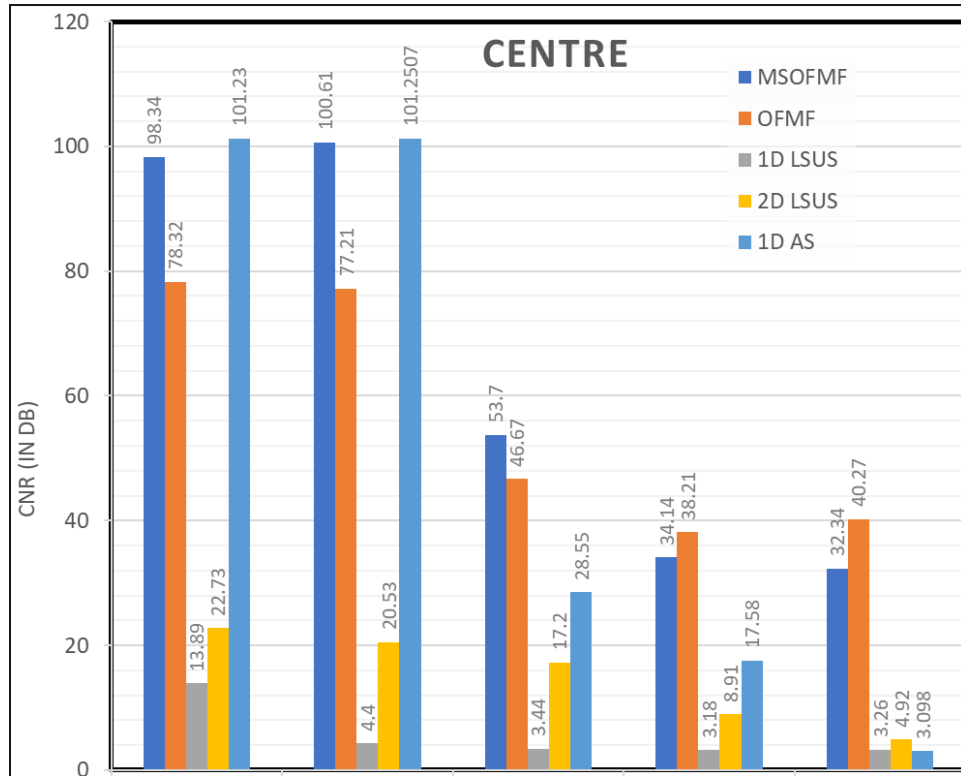


Fig. 4.8 CNR comparison of the centre inclusion.

The table below displays the various CNR values determined by the aforementioned algorithms for the centre inclusion.

Table 4.4 CNR comparison of the centre inclusion.

	2% applied strain	4% applied strain	8% applied strain	12% applied strain	16% applied strain
MSOFMF	98.34	100.61	53.7	34.14	32.34
OFMF	78.32	77.21	46.67	38.21	40.27
1D LSUS	13.89	4.4	3.44	3.18	3.26
2D LSUS	22.73	20.53	17.2	8.91	4.92
1D AS	101.23	101.2507	28.55	17.58	3.098

4.1.3.2.3 Bottom Left Inclusion

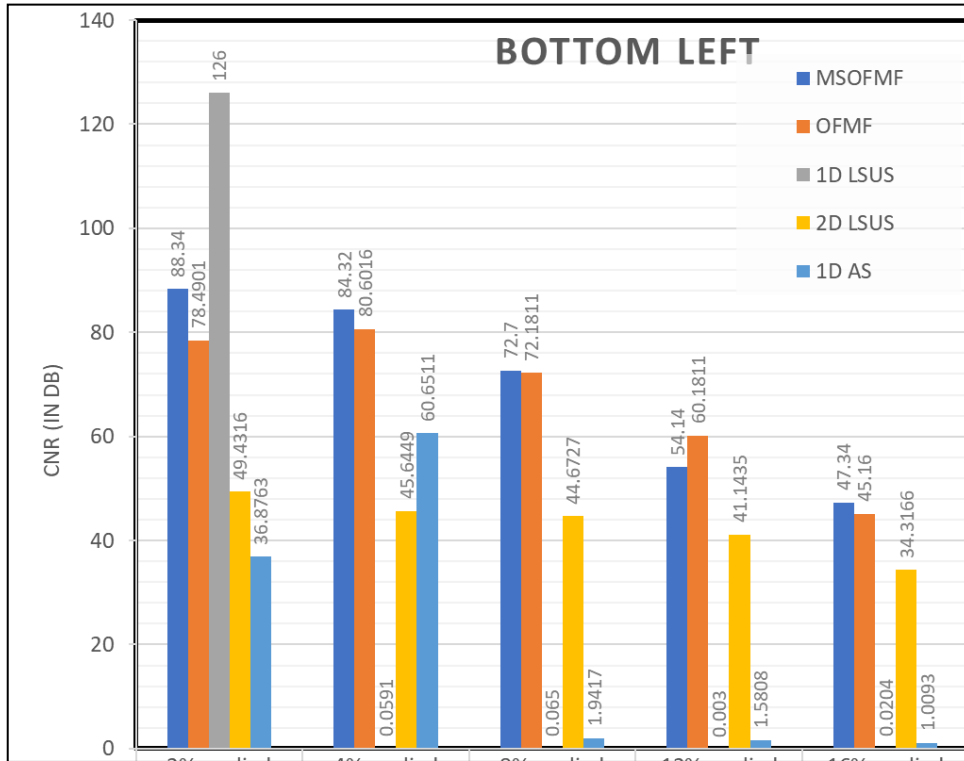


Fig. 4.9 CNR comparison of the bottom left inclusion.

Table 4.5 depicts the various CNR values determined by the algorithms for the bottom left inclusion.

Table 4.5 CNR comparison of the bottom left inclusion.

	2% applied strain	4% applied strain	8% applied strain	12% applied strain	16% applied strain
MSOFMF	88.34	84.32	72.7	54.14	47.34
OFMF	78.4901	80.6016	72.1811	60.1811	45.16
1D LSUS	126	0.0591	0.065	0.003	0.0204
2D LSUS	49.4316	45.6449	44.6727	41.1435	34.3166
1D AS	36.8763	60.6511	1.9417	1.5808	1.0093

4.1.3.2.4 Bottom Right Inclusion

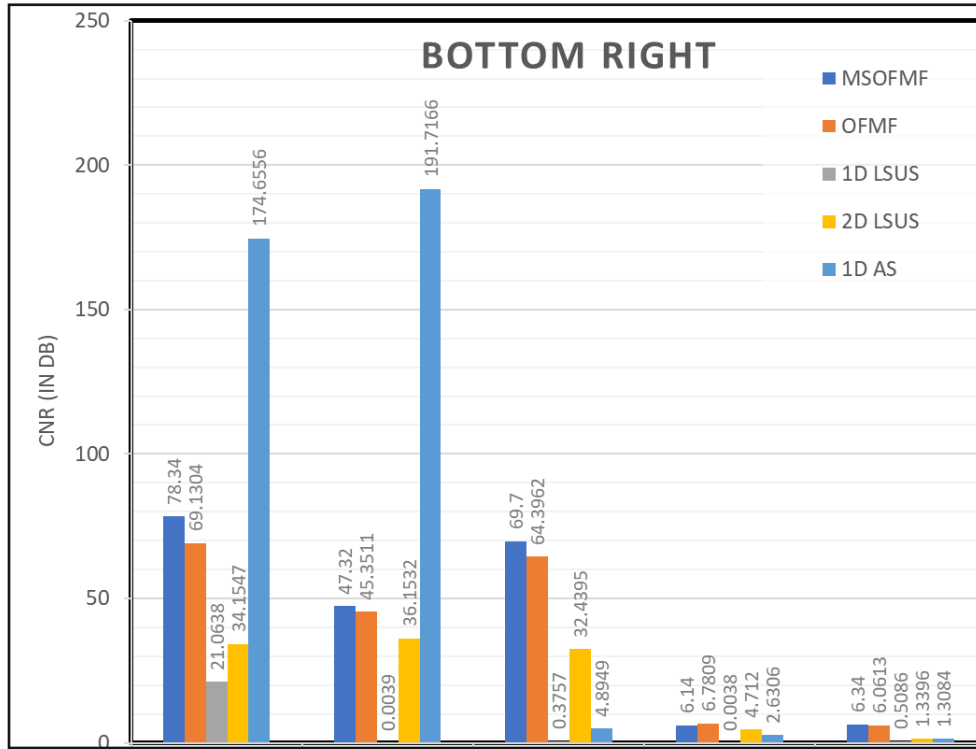


Fig. 4.10 CNR comparison of the bottom right inclusion.

Table 4.6 summarizes the various CNR values obtained by the different algorithms for the bottom right inclusion.

Table 4.6 CNR comparison of the bottom right inclusion.

	2% applied strain	4% applied strain	8% applied strain	12% applied strain	16% applied strain
MSOFMF	78.34	47.32	69.7	6.14	6.34
OFMF	69.1304	45.3511	64.3962	6.7809	6.0613
1D LSUS	21.0638	0.0039	0.3757	0.0038	0.5086
2D LSUS	34.1547	36.1532	32.4395	4.712	1.3396
1D AS	174.6556	191.7166	4.8949	2.6306	1.3084

4.1.4 Performance Analysis

The 2nd proposed technique, i.e., MSOFMF strain estimator outperforms all other strain estimators in the SNR Comparison while OFMF is a close second. In terms of CNR, MSOFMF technique performs similarly apart from the bottom right lesion. In the bottom right boundaries, our estimator performs slightly bad. This is not a major concern as lesion generally appears in the middle of the screen in cases of patient data.

4.2 Patient Data/In-vivo Data

In this section, we present ultrasound elastograms of in-vivo breast data using our algorithm and well-known algorithms. A database of 33 cases which were acquired by using a Sonix SP500 (Ultrasonix Medical Corporation, Richmond, BC, Canada) scanner integrated with an L14–5/38 probe operating at 10 MHz (nominal) at the University of Vermont Medical Center is used for this study. Free-hand compression was used for the acquisition of data. In this database, the age of the patients varied from 20 to 75 years. The database consists of cases that are both benign, i.e., fibroadenomas, and malignant, i.e., adenocarcinomas.

4.2.1 Processing Parameters

The frame size after the conversion of RF echo signal to B-mode is 2392 pixels *128 A-lines. Axially the pixel separation equals 37 micrometers. The processing parameters are selected empirically according to our prior experiences to maximize the cross-correlation function. The processing parameters used in our 2nd proposed technique MSOFMF strain estimator are summarized in the Table 4.7.

Table 4.7 Processing parameters at different stages of multistage motion estimation.

	1 st stage	2 nd stage	3 rd stage
Kernel	128 x 16	64 x 8	32 x 6
Search Window	192 x 24	86 x 12	44 x 8
Shift	32 x 2	32 x 2	16 x 2
Lag restriction	–	$\pm 10 \times \pm 2$	$\pm 4 \times \pm 2$

For the first proposed technique OFMF strain estimator, first-stage processing parameters of table 4.1 were used for motion estimation. A detailed comparison between the proposed methods and other well-established strain estimators for the 4 cases out of the 33 cases of the patient database algorithms is presented below. Fig. 4.11-Fig. 4.14 illustrate the log compressed B-mode image along with the elastograms of various known algorithms for comparison for patient 1-patient 4 respectively.

4.2.2 Patient 1

Patient 1 is a 34 years-old lady. She had a 14x10x14mm lesion in her left breast. Histopathological reports indicate this case is a fibroadenoma.

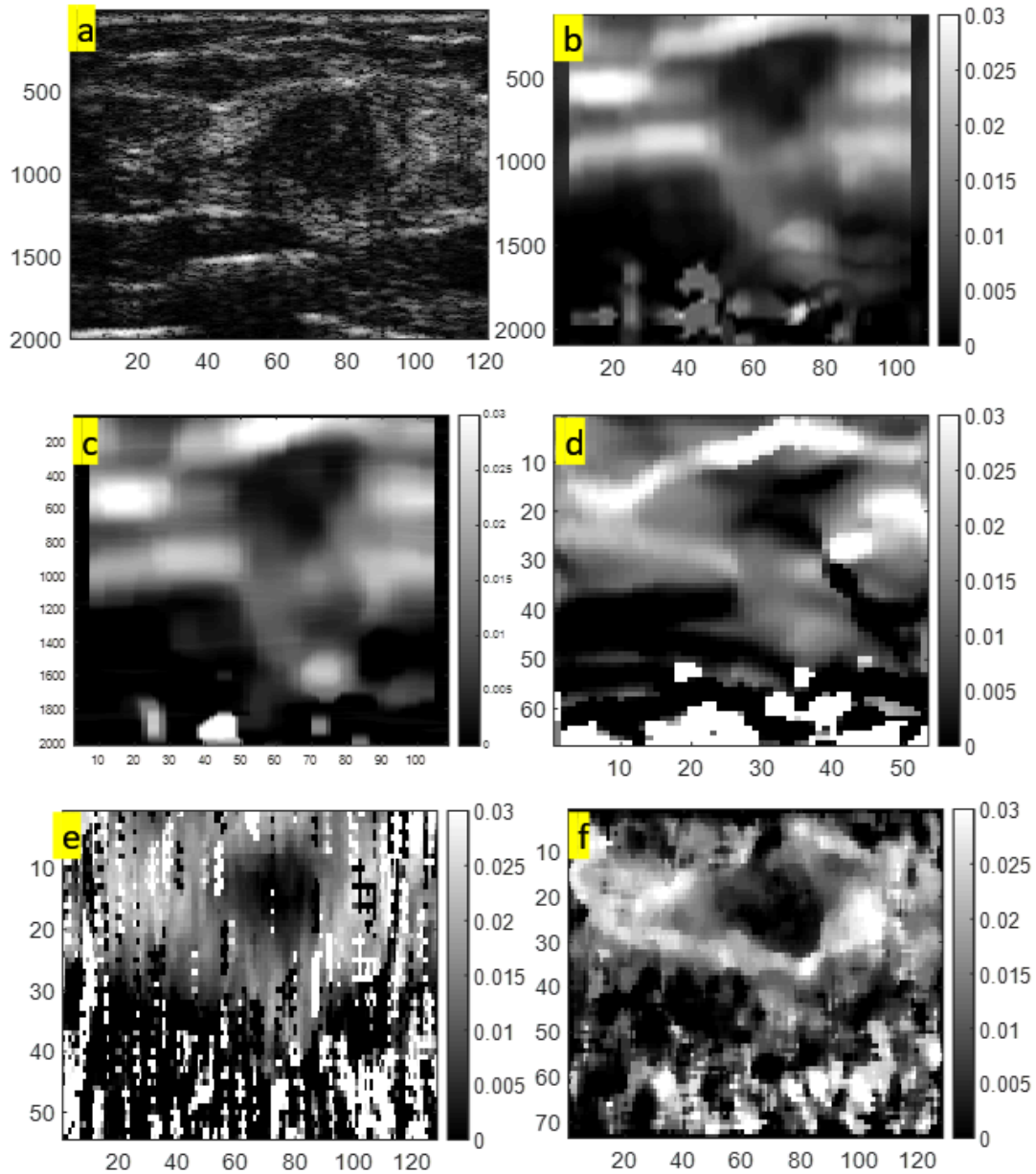


Fig. 4.11 Patient 1-(a). Log compressed B-mode image, Elastogram using - (b) MSOFMF (c) OFMF (d) 2D least squares method with uniform temporal stretching, (e) 1D least squares method with uniform temporal stretching (f) 1D spectral adaptive stretching strain estimators.

4.2.3 Patient 2

Patient 2 is a 53-year-old lady. She had a recurrence of breast cancer in her right breast after dense hyalinized interlobular fibrosis. The lesion was 10x8x5mm, and histopathological reports confirm that this case was also adenocarcinoma, i.e., malignant.

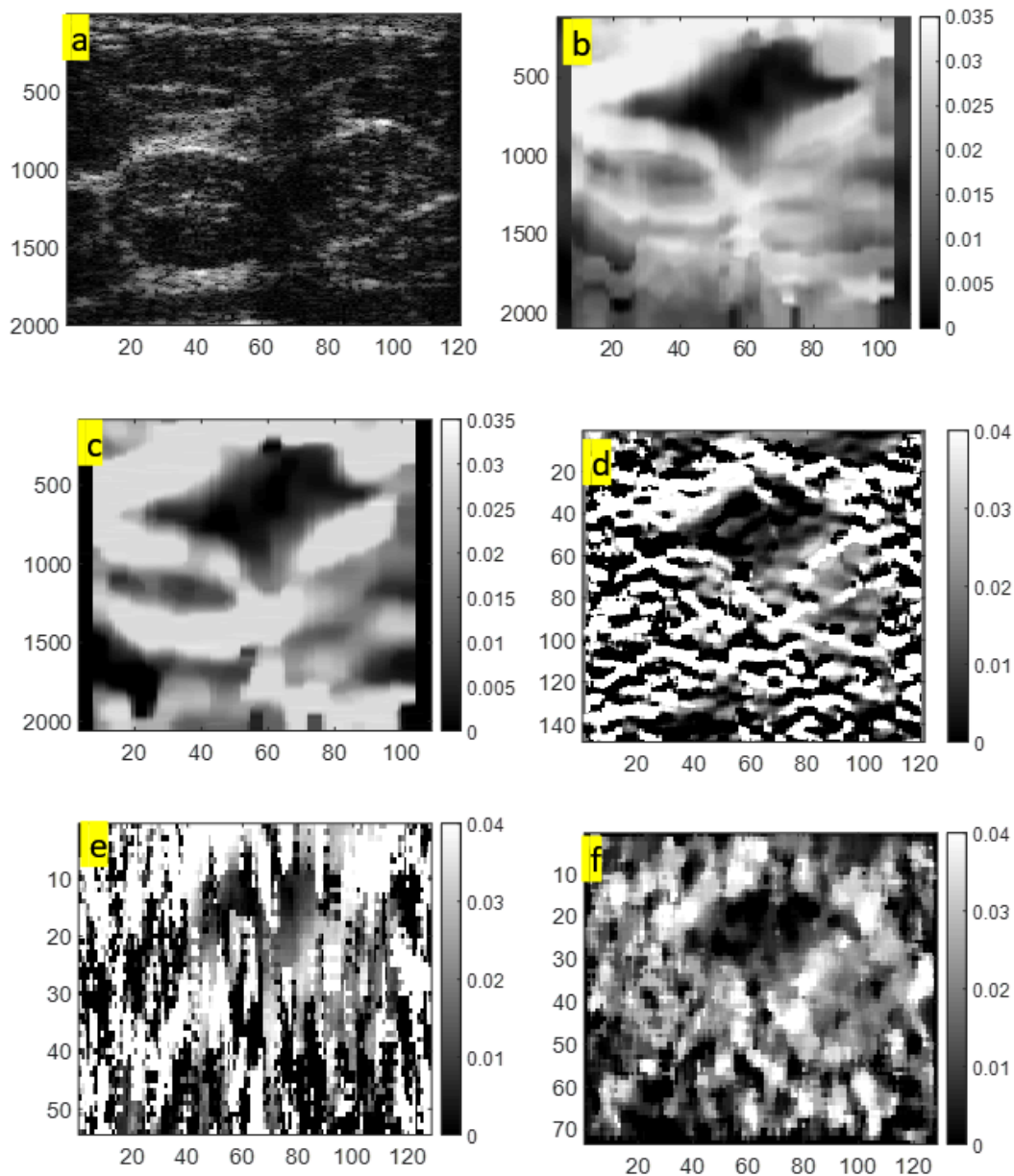


Fig. 4.12 Patient 2-(a). Log compressed B-mode image, - (a). Log compressed B-mode image, Elastogram using - (b) MSOFMF (c) OFMF (d) 2D least squares method with uniform temporal stretching, (e) 1D least squares method with uniform temporal stretching (f) 1D spectral adaptive stretching strain estimators.

4.2.4 Patient 3

Patient 3 is a 70-year-old lady with a malignant lesion of 10x7x11mm in her left breast. Histopathological reports approve that this is a case of adenocarcinoma.

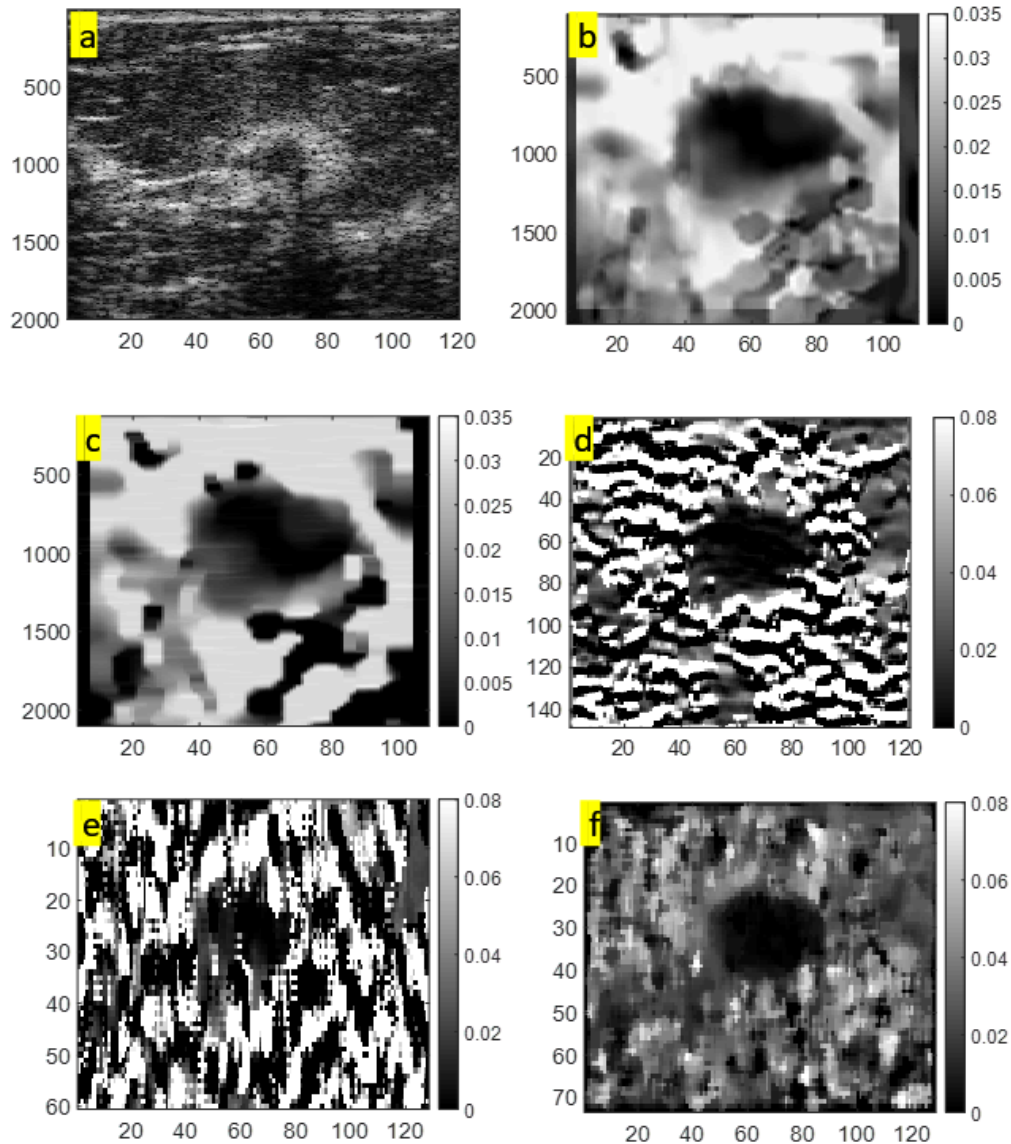


Fig. 4.13 Patient 3-(a). Log compressed B-mode image, Elastogram using - (b) MSOFMF (c) OFMF (d) 2D least squares method with uniform temporal stretching, (e) 1D least squares method with uniform temporal stretching (f) 1D spectral adaptive stretching strain estimators.

4.2.5 Patient 4

Patient 4 was a 64-year-old lady at the time of data acquisition. She had a 3x4x3mm invasive ductal adenocarcinoma according to the histopathological reports.

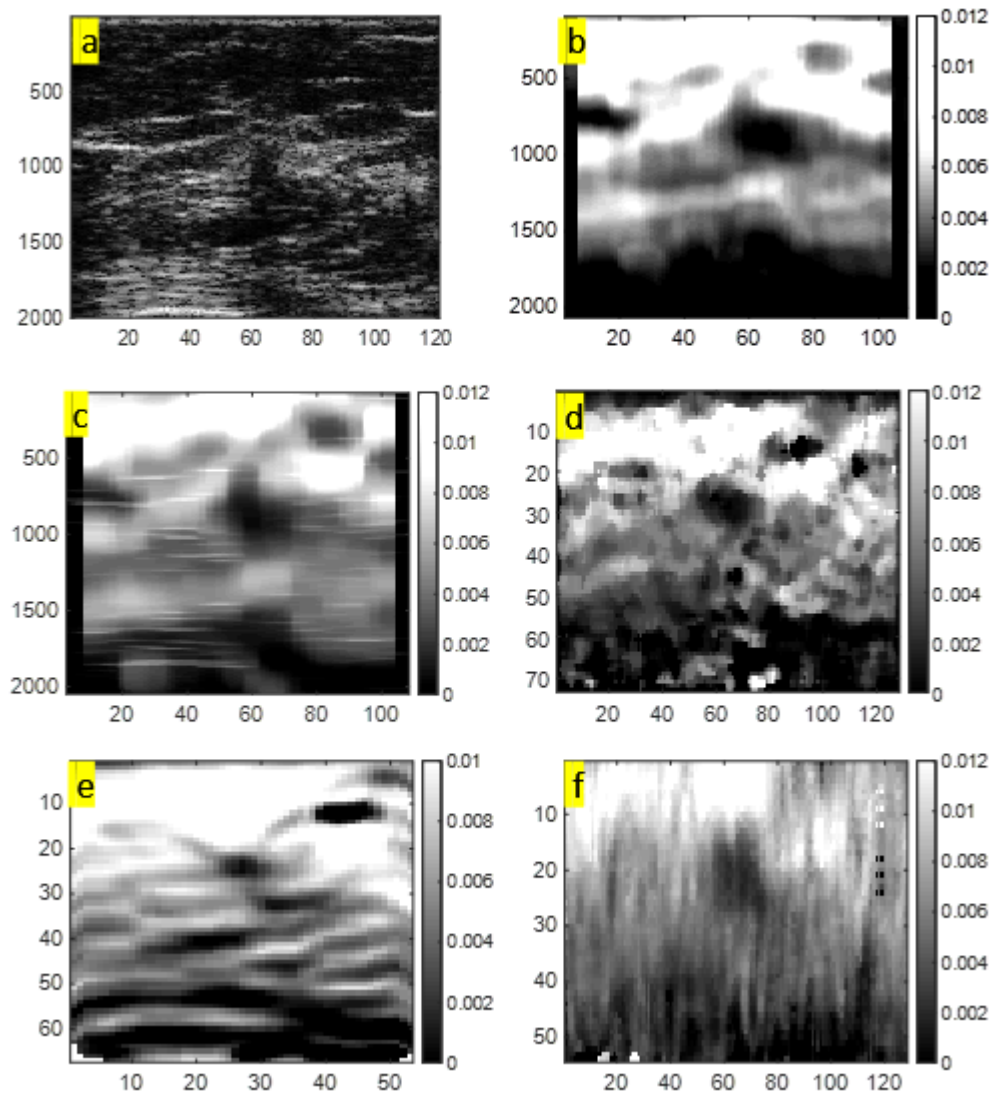


Fig. 4.14 Patient 4-(a). Log compressed B-mode image, Elastogram using - (b) MSOFMF (c) OFMF (d) 2D least squares method with uniform temporal stretching, (e) 1D least squares method with uniform temporal stretching (f) 1D spectral adaptive stretching strain estimators.

4.2.6 Performance Analysis

The SNR of the elastograms of 4 patient cases implemented by MSOFMF strain estimator, OFMF strain estimator, 2D least-squares strain estimator with uniform temporal stretching, 1D least-squares strain estimator with uniform temporal stretching, 1D spectral adaptive stretching strain estimator is documented in the chart of Fig. 4.15. It is evident that both of our proposed techniques outperform the other techniques by a good margin.

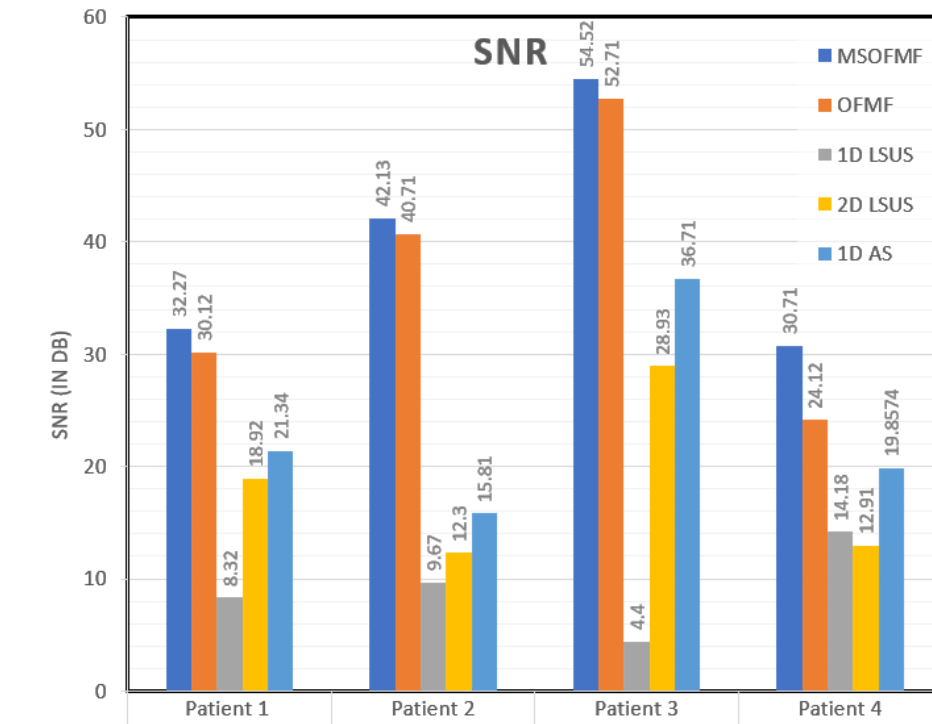


Fig. 4.15 SNR comparison of patient data cases.

The chart can be summarized in the Table 4.8.

Table 4.8 SNR comparison of patient data cases

	Patient 1	Patient 2	Patient 3	Patient 4
MSOFMF	32.27	42.13	54.52	30.71
OFMF	30.12	40.71	52.71	24.12
1D LSUS	8.32	9.67	4.4	14.18
2D LSUS	18.92	12.3	28.93	12.91
1D AS	21.34	15.81	36.71	19.8574

Chapter 5

DISCUSSION and CONCLUSION

5.1 Discussions

We have introduced two methods of generating strain elastograms using multiple frames from data acquisition. Our first technique, “Optical flow-based multi-frame strain estimator,” is based on optical flow and multiple frames. This algorithm was further improved by the addition of multistage displacement estimation before the implementation of the multi-frame optical flow layer. Both algorithms produce better quality elastograms using only B-mode data. In contrast, conventional algorithms use RF data that is more computationally expensive due to the rapid fluctuation nature of the acquisition of data and is prone to signal decorrelation.

In both the proposed techniques motion estimation through block matching is only performed once between frames 1 and frame 2 and that initial motion is used later to obtain finer motion between frame 2 and frame 3. These finer motions are then used to obtain frame sized strain estimates using registration techniques. The conventional multi frame algorithms typically compound the strain between frame pairs and average them which requires motion estimation twice and is more time consuming. It was shown that good performance can be achieved by estimating motion once using our algorithms.

The second technique MSOFMF strain estimator uses multistage motion tracking to improve the quality of strain elastograms even further. This algorithm takes more time to execute than OFMF strain estimator due to the multi-stage motion estimation. 3 stages of guided block matching were executed with smaller processing parameters at higher stages to estimate the motion finely. The displacements to be tracked at the end of the multistage estimation are very small and trying to estimate that motion through higher stage in the multistage hierarchy leads to decorrelation. As a result, to achieve optimal performance the residual finer motion is estimated through Horn Shunck optical flow. Consequent unwarping and warping of frame 2 with the motion estimates from last stage of the multistage displacement estimation aids in mapping the finer motion in the strain map resulting in better performance metrics.

In chapter 4, it has been established that the proposed methods perform better than the other well-established methods like adaptive stretching, 1D Least square estimator, 2D least square estimator with temporal extension, etc.

5.2 Conclusion

The desired outcomes of a strain estimation algorithm suited for ultrasound elastography are accuracy of motion estimation, higher resolution, robustness to noise and decorrelation arising from out of plane motion, faster execution speeds, and precision to be integrated into subsequent quantitative analysis algorithms. The techniques were proposed to work on these aforementioned aspects.

The strain images generated with proposed algorithms provide a better visual depiction of the presence of lesions. In comparison to other algorithms, the strain pictures demarcate lesion borders with reduced background noise. Even at higher applied strains, such as 12 and 16 percent in simulations, the suggested strain estimators clearly demarcate all the lesion without knowing or estimation of the applied strain. This not only demonstrates that our algorithms are resilient to increasing noise, but it also demonstrates that they are more suited to subsequent segmentation and quantitative approaches.

Increasing resolution has always been a challenge in ultrasound elastography. The increased spatial resolution makes strain elastograms suitable for modern display technologies and makes sequential computer-aided diagnosis through segmentation and quantitative analysis computationally easier. The proposed techniques are capable of increasing the spatial resolution by a factor of ~ 30 than the other algorithms making elastograms similar to frame size.

Higher performance parameters like increased SNR and CNR are good indications of the efficacy of the algorithm. Higher SNR and CNR have been achieved with the added benefit of increased resolution and less computational expense through using only B-mode data.

5.3 Future Perspectives

The techniques proposed in this thesis work are based on CPU utilization. Although we were able to set benchmarks in terms of the quality of strain images, our algorithm can be implemented with GPU coding in the future to make it even computationally less time-consuming and real-time.

This work has been based on an empirical selection of good frames from a known patient database. For newer data sets, the prior knowledge of selecting good knowledge may not yield good output. Thus, a machine learning algorithm can be incorporated to know the good frames for implementing the multiple frame-based algorithms. Modern machine learning algorithms need high volumes of labeled data to perform well. Due to our limitation of the infrastructure to collect real-time patient data in Bangladesh, training machine learning-based neural networks will be very hard. But in the future, the availability of the training data labeled by expert radiologists, would help to progress the research in this area.

References

- [1] J. Ophir, "Elastography: A quantitative method for imaging the elasticity of biological tissues," *Ultrason. Imaging*, vol. 13, no. 2, pp. 111–134, Apr. 1991, doi: 10.1016/0161-7346(91)90079-w.
- [2] T. Varghese, "Quasi-Static Ultrasound Elastography," *Ultrasound Clinics*, vol. 4, no. 3. NIH Public Access, pp. 323–338, Jul. 2009, doi: 10.1016/j.cult.2009.10.009.
- [3] H. E. RESINGER, "Radiation pathology.," *J. Iowa State Med. Soc.*, vol. 52, pp. 404–406, 1962, doi: 10.5005/jp/books/12793_3.
- [4] K. E and O. J, "A new elastographic method for estimation and imaging of lateral displacements, lateral strains, corrected axial strains and Poisson's ratios in tissues," *Ultrasound Med. Biol.*, vol. 24, no. 8, pp. 1183–1199, Oct. 1998, doi: 10.1016/S0301-5629(98)00109-4.
- [5] M. Bilgen and M. F. Insana, "Deformation models and correlation analysis in elastography," *J. Acoust. Soc. Am.*, vol. 99, no. 5, pp. 3212–3224, May 1996, doi: 10.1121/1.414865.
- [6] M. A. Hussain, E. M. Abu Anas, S. K. Alam, S. Y. Lee, and M. K. Hasan, "Direct and gradient-based average strain estimation by using weighted nearest neighbor cross-correlation peaks," *IEEE Trans. Ultrason. Ferroelectr. Freq. Control*, vol. 59, no. 8, pp. 1713–1728, 2012, doi: 10.1109/TUFFC.2012.2376.
- [7] R. Ahmed *et al.*, "Comparison of windowing effects on elastography images: Simulation, phantom and in vivo studies," *Ultrasonics*, vol. 66, pp. 140–153, Mar. 2016, doi: 10.1016/j.ultras.2015.11.001.
- [8] E. E. Konofagou, T. Varghese, and J. Ophir, "Spectral estimators in elastography," *Ultrasonics*, vol. 38, no. 1, pp. 412–416, Mar. 2000, doi: 10.1016/S0041-624X(99)00116-X.
- [9] M. K. Hasan, E. M. A. Anas, S. K. Alam, and S. Y. Lee, "Direct Mean Strain Estimation for Elastography Using Nearest-Neighbor Weighted Least-Squares Approach in the Frequency Domain," *Ultrasound Med. Biol.*, vol. 38, no. 10, pp. 1759–1777, Oct. 2012, doi: 10.1016/j.ultrasmedbio.2012.01.026.
- [10] S. Kaiser Alam, J. Ophir, and T. Varghese, "Elastographic axial resolution criteria: An

- experimental study,” *IEEE Trans. Ultrason. Ferroelectr. Freq. Control*, vol. 47, no. 1, pp. 304–309, 2000, doi: 10.1109/58.818775.
- [11] H. Rivaz, E. M. Boctor, M. A. Choti, and G. D. Hager, “Ultrasound elastography using three images,” in *Lecture Notes in Computer Science (including subseries Lecture Notes in Artificial Intelligence and Lecture Notes in Bioinformatics)*, 2011, vol. 6891 LNCS, no. PART 1, pp. 371–378, doi: 10.1007/978-3-642-23623-5_47.
- [12] H. Rivaz, E. M. Boctor, M. A. Choti, and G. D. Hager, “Ultrasound elastography using multiple images,” *Med. Image Anal.*, vol. 18, no. 2, pp. 314–329, Feb. 2014, doi: 10.1016/j.media.2013.11.002.
- [13] M. O’Donnell, A. R. Skovoroda, B. M. Shapo, and S. Y. Emelianov, “Internal Displacement and Strain Imaging Using Ultrasonic Speckle Tracking,” *IEEE Trans. Ultrason. Ferroelectr. Freq. Control*, vol. 41, no. 3, pp. 314–325, 1994, doi: 10.1109/58.285465.
- [14] K. Hoyt, F. Forsberg, and J. Ophir, “Analysis of a hybrid spectral strain estimation technique in elastography,” *Phys. Med. Biol.*, vol. 51, no. 2, pp. 197–209, Jan. 2006, doi: 10.1088/0031-9155/51/2/001.
- [15] X. Pan, J. Gao, S. Tao, K. Liu, J. Bai, and J. Luo, “A two-step optical flow method for strain estimation in elastography: Simulation and phantom study,” *Ultrasonics*, vol. 54, no. 4, pp. 990–996, Apr. 2014, doi: 10.1016/j.ultras.2013.11.010.
- [16] A. R. Amiri-Simkooei, M. Hosseini-Asl, and A. Safari, “Least squares 2D bi-cubic spline approximation: Theory and applications,” *Meas. J. Int. Meas. Confed.*, vol. 127, pp. 366–378, Oct. 2018, doi: 10.1016/j.measurement.2018.06.005.
- [17] S. R. Ara *et al.*, “Phase-based direct average strain estimation for elastography,” *IEEE Trans. Ultrason. Ferroelectr. Freq. Control*, vol. 60, no. 11, pp. 2266–2283, 2013, doi: 10.1109/TUFFC.2013.6644732.
- [18] T. Varghese, “Quasi-Static Ultrasound Elastography,” *Ultrasound Clin.*, vol. 4, no. 3, p. 323, Jul. 2009, doi: 10.1016/J.CULT.2009.10.009.
- [19] I. Céspedes, J. Ophir, and M. Insana, “Theoretical Bounds on Strain Estimation in Elastography,” *IEEE Trans. Ultrason. Ferroelectr. Freq. Control*, vol. 42, no. 5, pp. 969–971, 1995, doi: 10.1109/58.464850.

- [20] J. Y. Kwak and E. K. Kim, “Ultrasound elastography for thyroid nodules: Recent advances,” *Ultrasonography*, vol. 33, no. 2. Korean Society of Ultrasound in Medicine, pp. 75–82, Feb. 26, 2014, doi: 10.14366/usg.13025.
- [21] S. Il Hwang, H. J. Lee, S. E. Lee, S. K. Hong, S.-S. Byun, and G. Choe, “Elastographic Strain Index in the Evaluation of Focal Lesions Detected With Transrectal Sonography of the Prostate Gland,” *J. Ultrasound Med.*, vol. 35, no. 5, pp. 899–904, May 2016, doi: 10.7863/ULTRA.15.01071.
- [22] H. Singh, O. B. Panta, U. Khanal, and R. K. Ghimire, “Renal Cortical Elastography: Normal Values and Variations,” *J. Med. Ultrasound*, vol. 25, no. 4, p. 215, Dec. 2017, doi: 10.1016/J.JMU.2017.04.003.
- [23] A. T. Ahuja *et al.*, “Ultrasound of malignant cervical lymph nodes,” *Cancer Imaging*, vol. 8, no. 1. BioMed Central, pp. 48–56, 2008, doi: 10.1102/1470-7330.2008.0006.
- [24] S. Iranmakani *et al.*, “A review of various modalities in breast imaging: technical aspects and clinical outcomes,” *Egypt. J. Radiol. Nucl. Med. 2020 511*, vol. 51, no. 1, pp. 1–22, Apr. 2020, doi: 10.1186/S43055-020-00175-5.
- [25] K. M. Hiltawsky, M. Krüger, C. Starke, L. Heuser, H. Ermert, and A. Jensen, “Freehand ultrasound elastography of breast lesions: Clinical results,” *Ultrasound Med. Biol.*, vol. 27, no. 11, pp. 1461–1469, 2001, doi: 10.1016/S0301-5629(01)00434-3.
- [26] I. Céspedes, J. Ophir, H. Ponnekanti, and N. Maklad, “Elastography: Elasticity Imaging Using Ultrasound with Application to Muscle and Breast in Vivo:,” <http://dx.doi.org/10.1177/016173469301500201>, vol. 15, no. 2, pp. 73–88, Aug. 2016, doi: 10.1177/016173469301500201.
- [27] B. Mahmood, C. Ewertsen, J. Carlsen, and M. B. Nielsen, “Ultrasound Vascular Elastography as a Tool for Assessing Atherosclerotic Plaques – A Systematic Literature Review,” *Ultrasound Int. Open*, vol. 2, no. 4, p. E106, Nov. 2016, doi: 10.1055/S-0042-115564.
- [28] F. Pinto *et al.*, “Imaging in prostate cancer diagnosis: Present role and future perspectives,” *Urol. Int.*, vol. 86, no. 4, pp. 373–382, Jun. 2011, doi: 10.1159/000324515.
- [29] G. Salomon and J. Schiffmann, “Real-time elastography for the detection of prostate

- cancer,” *Curr. Urol. Rep.*, vol. 15, no. 3, 2014.
- [30] T. DJ *et al.*, “Elastography in prostate gland imaging and prostate cancer detection,” *Med. Ultrason.*, vol. 20, no. 4, pp. 515–523, 2018, doi: 10.11152/MU-1655.
- [31] J. Ophir *et al.*, “Elastography: Ultrasonic estimation and imaging of the elastic properties of tissues,” *Proc. Inst. Mech. Eng. Part H J. Eng. Med.*, vol. 213, no. 3, pp. 203–233, 1999, doi: 10.1243/0954411991534933.
- [32] S. K. Alam and J. Ophir, “Reduction of signal decorrelation from mechanical compression of tissues by temporal stretching: Applications to elastography,” *Ultrasound Med. Biol.*, vol. 23, no. 1, pp. 95–105, Jan. 1997, doi: 10.1016/S0301-5629(96)00164-0.
- [33] S. K. Alam, F. L. Lizzi, T. Varghese, E. J. Feleppa, and S. Ramachandran, “Adaptive spectral strain estimators for elastography,” *Ultrason. Imaging*, vol. 26, no. 3, pp. 131–149, Aug. 2004, doi: 10.1177/016173460402600301.
- [34] J. Jin, J. Zhang, and Y. Shen, “Adaptive stretch factor method based on moving window for ultrasound elasticity imaging,” *Yi Qi Yi Biao Xue Bao/Chinese J. Sci. Instrum.*, vol. 35, no. 9, pp. 2087–2093, 2014, Accessed: Jun. 28, 2021. [Online]. Available: https://www.researchgate.net/publication/288238024_Adaptive_stretch_factor_method_based_on_moving_window_for_ultrasound_elasticity_imaging.
- [35] E. Konofagou and J. Ophir, “A new elastographic method for estimation and imaging of lateral displacements, lateral strains, corrected axial strains and Poisson’s ratios in tissues,” *Ultrasound Med. Biol.*, vol. 24, no. 8, pp. 1183–1199, Oct. 1998, doi: 10.1016/S0301-5629(98)00109-4.
- [36] Z. Z, L. H, and C. Y, “2D ultrasonic elastography with lateral displacement estimation using statistics,” *Biomed. Mater. Eng.*, vol. 24, no. 6, pp. 2783–2791, 2014, doi: 10.3233/BME-141096.
- [37] J. Jiang and T. J. Hall, “A Coupled Subsample Displacement Estimation Method for Ultrasound-Based Strain Elastography,” *Phys. Med. Biol.*, vol. 60, no. 21, p. 8347, Oct. 2015, doi: 10.1088/0031-9155/60/21/8347.
- [38] M. A. Lubinski, S. Y. Emelianov, and M. O’Donnell, “Speckle tracking methods for ultrasonic elasticity imaging using short-time correlation,” *IEEE Trans. Ultrason.*

- Ferroelectr. Freq. Control*, vol. 46, no. 1, pp. 82–96, 1999, doi: 10.1109/58.741427.
- [39] H. Shi and T. Varghese, “Two-dimensional multi-level strain estimation for discontinuous tissue,” *Phys. Med. Biol.*, vol. 52, no. 2, pp. 389–401, Jan. 2007, doi: 10.1088/0031-9155/52/2/006.
- [40] N. H. Meshram and T. Varghese, “GPU accelerated multilevel lagrangian carotid strain imaging,” *IEEE Trans. Ultrason. Ferroelectr. Freq. Control*, vol. 65, no. 8, pp. 1370–1379, Aug. 2018, doi: 10.1109/TUFFC.2018.2841346.
- [41] F. Yeung, S. F. Levinson, and K. J. Parker, “Multilevel and motion model-based ultrasonic speckle tracking algorithms,” *Ultrasound Med. Biol.*, vol. 24, no. 3, pp. 427–441, Mar. 1998, doi: 10.1016/S0301-5629(97)00281-0.
- [42] S. Loncaric and Z. Majcencic, “Optical flow algorithm for cardiac motion estimation,” in *Annual International Conference of the IEEE Engineering in Medicine and Biology - Proceedings*, 2000, vol. 1, pp. 415–417, doi: 10.1109/iembs.2000.900762.
- [43] E. Brusseau *et al.*, “In vivo response to compression of 35 breast lesions observed with a two-dimensional locally regularized strain estimation method,” *Ultrasound Med. Biol.*, vol. 40, no. 2, pp. 300–312, Feb. 2014, doi: 10.1016/j.ultrasmedbio.2013.02.017.
- [44] S. K. Alam, F. L. Lizzi, T. Varghese, E. J. Feleppa, and S. Ramachandran, “Adaptive spectral strain estimators for elastography,” *Ultrason. Imaging*, vol. 26, no. 3, pp. 131–149, Aug. 2004, doi: 10.1177/016173460402600301.
- [45] A. Pesavento, “A time-efficient and accurate strain estimation concept for ultrasonic elastography using iterative phase zero estimation,” *IEEE Trans. Ultrason. Ferroelectr. Freq. Control*, vol. 46, no. 5, pp. 1057–1067, 1999, doi: 10.1109/58.796111.
- [46] E. Brusseau, C. Perrey, P. Delachartre, M. Vogt, D. Vray, and H. Ermert, “Axial strain imaging using a local estimation of the scaling factor from RF ultrasound signals,” *Ultrason. Imaging*, vol. 22, no. 2, pp. 95–107, 2000, doi: 10.1177/016173460002200202.
- [47] H. Rivaz, E. Boctor, P. Foroughi, R. Zellars, G. Fichtinger, and G. Hager, “Ultrasound Elastography: A Dynamic Programming Approach,” *IEEE Trans. Med. Imaging*, vol. 27, no. 10, p. 1373, 2008, doi: 10.1109/TMI.2008.917243.
- [48] H. Rivaz, E. M. Boctor, M. A. Choti, and G. D. Hager, “Real-time regularized ultrasound elastography,” *IEEE Trans. Med. Imaging*, vol. 30, no. 4, pp. 928–945, Apr. 2011, doi:

10.1109/TMI.2010.2091966.

- [49] A. Tekalp, “Digital video processing,” *Prentice Hall Press*, 2015, Accessed: Jul. 04, 2021. [Online]. Available: <https://dl.acm.org/doi/abs/10.5555/2843012>.
- [50] S. Loncaric and Z. Majcenic, “Optical flow algorithm for cardiac motion estimation,” in *Annual International Conference of the IEEE Engineering in Medicine and Biology - Proceedings*, 2000, vol. 1, pp. 415–417, doi: 10.1109/iembs.2000.900762.
- [51] V. Pretlová and V. Červený, “Bicubic spline smoothing of two-dimensional geophysical data,” *Stud. Geophys. Geod.*, vol. 20, no. 2, pp. 168–177, 1976, doi: 10.1007/BF01626049.
- [52] A. Kouibia and M. Pasadas, “Approximation of Surfaces by Fairness Bicubic Splines,” *Adv. Comput. Math. 2004 201*, vol. 20, no. 1, pp. 87–103, Jan. 2004, doi: 10.1023/A:1025805701726.
- [53] N. Zainudin *et al.*, “Horn Schunck Algorithm for Facial Expression Change Detection Classification,” *Int. J. Inf. Secur. Res.*, vol. 5, no. 3, pp. 574–581, Sep. 2015, doi: 10.20533/IJISR.2042.4639.2015.0066.
- [54] V. T and O. J, “A theoretical framework for performance characterization of elastography: the strain filter,” *IEEE Trans. Ultrason. Ferroelectr. Freq. Control*, vol. 44, no. 1, pp. 164–172, 1997, doi: 10.1109/58.585212.